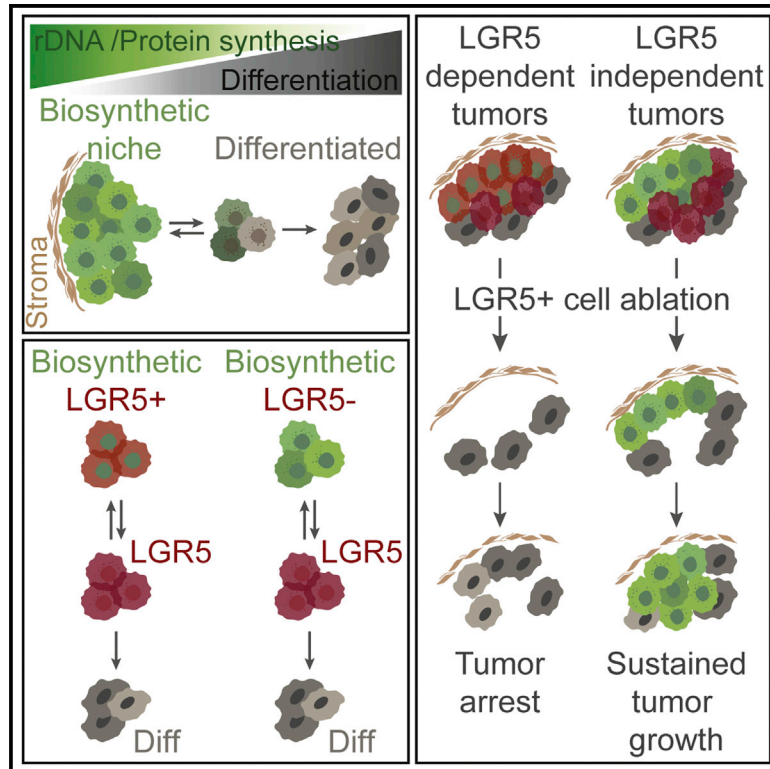


Zonation of Ribosomal DNA Transcription Defines a Stem Cell Hierarchy in Colorectal Cancer

Graphical Abstract



Authors

Clara Morral, Jelena Stanisavljevic, Xavier Hernando-Mombona, ..., Elena Sancho, Holger Heyn, Eduard Batlle

Correspondence

eduard.batlle@irbbarcelona.org

In Brief

Morral and colleagues discovered that most rRNA and proteins synthesized in colorectal cancers (CRCs) are contributed by a limited subset of tumor cells that reside adjacent to the stroma. This architecture defines a common stem cell hierarchy. In some CRCs, the biosynthetic tumor cell population renders LGR5⁺ tumor cells dispensable.

Highlights

- rRNA and proteins in CRCs are produced in dedicated tumor domains
- Differentiated tumor cells experience an irreversible loss of biosynthetic capacities
- POLR1A-high CRC cells reside at the top of the tumor cell hierarchy
- Both LGR5⁺ and LGR5⁻ tumor cells within biosynthetic niches fuel tumor growth

Article

Zonation of Ribosomal DNA Transcription Defines a Stem Cell Hierarchy in Colorectal Cancer

Clara Morral,^{1,10} Jelena Stanisavljevic,^{1,10} Xavier Hernando-Momblona,^{1,9} Elisabetta Mereu,² Adrián Álvarez-Varela,^{1,9} Carme Cortina,^{1,9} Diana Stork,¹ Felipe Slebe,¹ Gemma Turon,¹ Gavin Whissell,¹ Marta Sevillano,^{1,9} Anna Merlos-Suárez,¹ Àngela Casanova-Martí,¹ Catia Moutinho,² Scott W. Lowe,^{4,5} Lukas E. Dow,⁶ Alberto Villanueva,⁷ Elena Sancho,^{1,9} Holger Heyn,^{2,3} and Eduard Batlle^{1,8,9,11,*}

¹Institute for Research in Biomedicine (IRB Barcelona), Barcelona Institute of Science and Technology (BIST), Baldiri i Reixac 10, 08028 Barcelona, Spain

²CNAG-Centre for Genomic Regulation (CRG), BIST, Baldiri i Reixac 4, 08028 Barcelona, Spain

³Universitat Pompeu Fabra (UPF), Barcelona, Spain

⁴Department of Cancer Biology and Genetics, Memorial Sloan Kettering Cancer Center, New York, NY 10065, USA

⁵Howard Hughes Medical Institute, Chevy Chase, MD 20815, USA

⁶Department of Medicine, Weill-Cornell Medical College, New York, NY 10021, USA

⁷Group of Chemoresistance and Predictive Factors, Subprogram Against Cancer Therapeutic Resistance (ProCURE), ICO, Oncobell Program, IDIBELL, L'Hospitalet del Llobregat, 08908 Barcelona, Spain

⁸ICREA, Passeig Lluís Companys 23, 08010 Barcelona, Spain

⁹Centro de Investigación Biomédica en Red de Cáncer (CIBERONC), 08028 Barcelona, Spain

¹⁰These authors contributed equally

¹¹Lead Contact

*Correspondence: eduard.batlle@irbbarcelona.org

<https://doi.org/10.1016/j.stem.2020.04.012>

SUMMARY

Colorectal cancers (CRCs) are composed of an amalgam of cells with distinct genotypes and phenotypes. Here, we reveal a previously unappreciated heterogeneity in the biosynthetic capacities of CRC cells. We discover that the majority of ribosomal DNA transcription and protein synthesis in CRCs occurs in a limited subset of tumor cells that localize in defined niches. The rest of the tumor cells undergo an irreversible loss of their biosynthetic capacities as a consequence of differentiation. Cancer cells within the biosynthetic domains are characterized by elevated levels of the RNA polymerase I subunit A (POLR1A). Genetic ablation of POLR1A-high cell population imposes an irreversible growth arrest on CRCs. We show that elevated biosynthesis defines stemness in both LGR5⁺ and LGR5⁻ tumor cells. Therefore, a common architecture in CRCs is a simple cell hierarchy based on the differential capacity to transcribe ribosomal DNA and synthesize proteins.

INTRODUCTION

Only subsets of tumor cells isolated from colorectal cancer (CRC) samples, the so-called cancer stem cells (CSCs), display tumorigenic potential upon transplantation into recipient mice (Dalerba et al., 2007; Merlos-Suárez et al., 2011; O'Brien et al., 2007; Ricci-Vitiani et al., 2007; Vermeulen et al., 2010). This finding led to the notion that CRCs are organized according to a stem cell hierarchy. Tumor cells present in full-blown CRCs echo the phenotypes observed in healthy colonic mucosa, including stem cell-like and differentiated-like states characterized by expression programs reminiscent of those present in their normal counterparts (Dalerba et al., 2011; Merlos-Suárez et al., 2011; Vermeulen et al., 2008). Lineage-tracing experiments in xenografts demonstrated that LGR5⁺ stem cell-like tumor cells exhibit long-term self-renewal and differentiation capacities, whereas KRT20⁺ differentiated cells produce mostly

short-lived progeny (Cortina et al., 2017; Shimokawa et al., 2017). However, genetic ablation of LGR5⁺ cells in these cancer models triggers a regenerative response by which LGR5⁻ tumor cells convert to an LGR5⁺ state and regenerate the CSC pool (Shimokawa et al., 2017; de Sousa e Melo et al., 2017). In addition, de Sauvage and colleagues showed that ablation of LGR5⁺ cells does not impair primary CRC growth, yet these cells are necessary for the expansion of metastases (de Sousa e Melo et al., 2017). These studies raise a number of important caveats. In particular, CSCs have been recognized by the expression of stem cell marker gene LGR5, yet many CRCs contain few or no LGR5⁺ cells (Merlos-Suárez et al., 2011; Shimokawa et al., 2017). It is unclear whether these LGR5⁻ CRCs still rely on a CSC hierarchy. One possibility is that CSCs may not be simply defined by LGR5 expression in some CRCs or even that particular tumors may contain LGR5⁺ and LGR5⁻ CSC subsets. Furthermore, although evidence supporting tumor cell plasticity

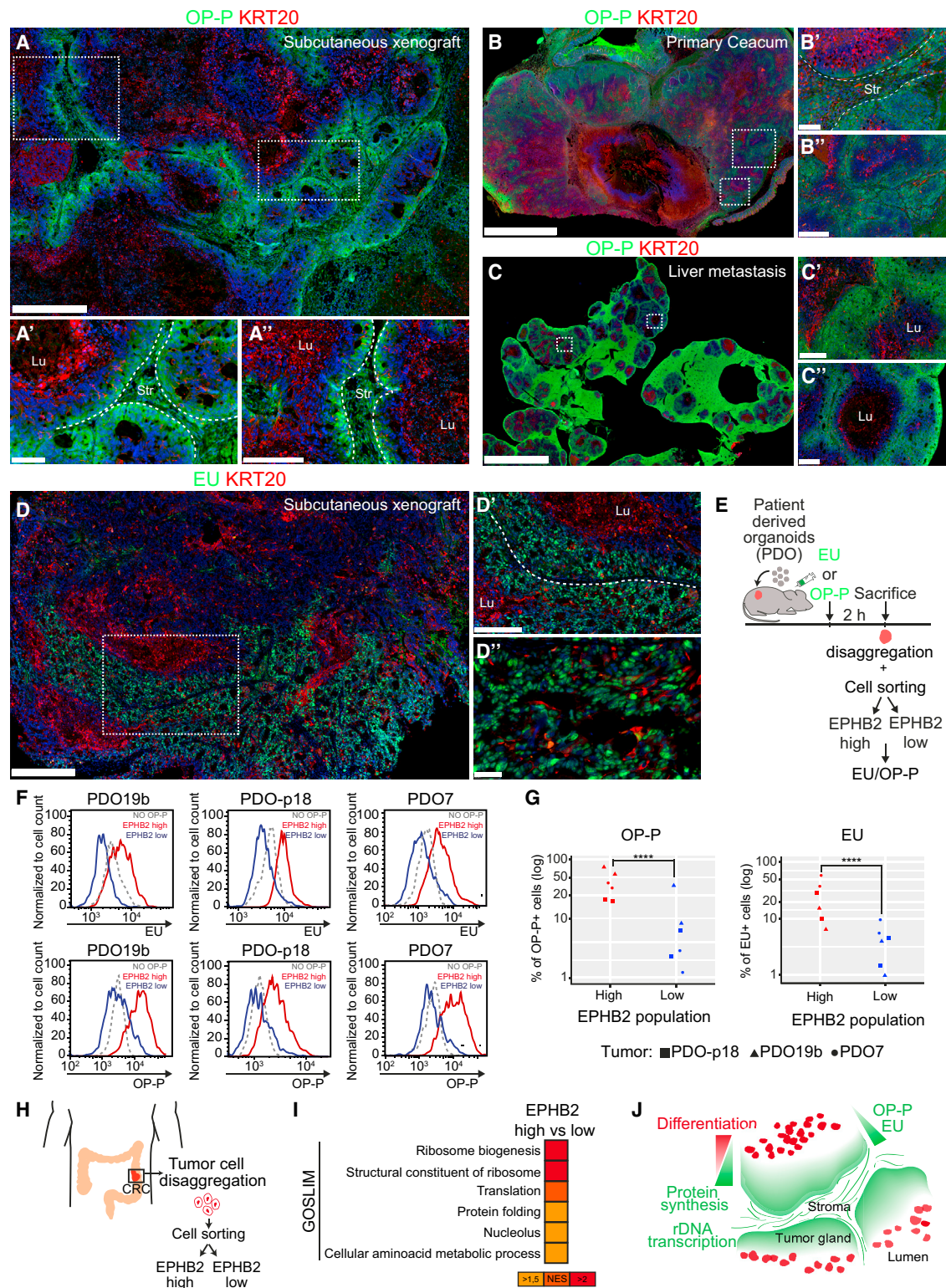


Figure 1. rDNA Transcription and Protein Synthesis across Different Models of CRC

(A) OP-P incorporation in a patient-derived xenograft (PDX). Lu, lumen; Str, stroma. Scale bars: (A), 500 μ m; (A'), 100 μ m; (A''), 250 μ m. Dashed lines outline the epithelial glands.

(B) OP-P incorporation in primary human CRC implanted orthotopically in mice. Str, stroma. Scale bars: (B), 2.5 mm; (B'), 100 μ m; (B''), 250 μ m. Dashed lines outline the epithelial glands.

(legend continued on next page)

is well established, it remains unknown whether all cell types present in CRCs are equally capable of regenerating the CSC pool. We reasoned that understanding the functions that characterize CSCs beyond the expression of marker genes may help to address these important issues.

While characterizing the properties of CSCs, we found that most rRNA and proteins synthesized in CRCs are contributed by a limited subset of cells that reside immediately adjacent to the stroma. In contrast, as tumor cells undergo differentiation, they experience an irreversible loss of rRNA and protein synthesis capacity. By exploring these unexpected findings, we demonstrate that zonation patterns of rDNA transcription and protein synthesis in CRC reflect the existence of a simple stem cell-like hierarchy based on the differential biosynthetic capacity of tumor cells.

RESULTS

Zonation of rRNA and Protein Synthesis in CRCs

We discovered striking zonation patterns of protein and ribosomal RNA (rRNA) synthesis in CRCs. O-propargyl-puromycin (OP-P) is a puromycin analog that is incorporated into nascent polypeptides (Blanco et al., 2016; Liu et al., 2012; Signer et al., 2014). In CRC patient-derived xenografts (PDXs), the OP-P⁺ domain was visualized as strings of cells adjacent to the stroma that surrounds each tumor gland (Figure 1A). Closer inspection confirmed that OP-P incorporation was largely restricted to tumor cells occupying basal positions, with the highest protein synthesis rates corresponding to those cells in closest proximity to the underlying mesenchyme, whereas cells that reside outside these domains, including KRT20⁺ differentiated tumor cells, did not incorporate OP-P (Figures 1A' and 1A''). Stromal cells stained strongly for OP-P. These OP-P zonation patterns were present in all xenografts analyzed, which included subcutaneous, orthotopic, and metastatic CRC models (examples in Figures 1B, 1C, S1A, and S1B). We also measured rDNA transcription by inoculating mice with 5-ethynyl uridine (EU), a ribonucleotide analog that can be visualized using click chemistry (Jao and Salic, 2008). EU incorporates mainly into rRNA (Jao and Salic, 2008), and, similar to OP-P, it labeled preferentially the nucleoli of tumor cells located adjacent to tumor stroma after a 2-h pulse (Figures 1D, 1D', 1D'', S1C, and S1D).

We next searched for surface marker genes that overlapped with the CRC biosynthetic zones identified above. In CRCs, the highest EPHB2 levels are expressed by a subset of undifferentiated tumor cells that reside in proximity to the stroma (Batlle et al., 2002; Merlos-Suárez et al., 2011). EPHB2-high cells resided within OP-P⁺ tumor domains (Figures S1E and S1F). Flow cytometry of dissociated xenografts demonstrated that

EU and OP-P incorporation was largely restricted to EPHB2-high tumor cells and further confirmed that most EPHB2-low tumor cells exhibited near-zero rDNA transcription and protein synthesis rates (Figures 1E and 1F). We obtained similar measurements in three xenografts from tumors with distinct genotypes (Figure 1G). We also performed transcriptional profiling of tumor cells purified from fresh surgical CRC specimens according to EPHB2 surface levels (n = 10) (Figure 1H). This study confirmed significant enrichment in gene sets associated to rRNA and protein synthesis in EPHB2-high compared to EPHB2-low tumor cells in all samples (Figure 1I; Table S6). Overall, these findings imply the existence of well-defined biosynthetic domains in CRC dedicated to producing rRNA and proteins (Figure 1J). This organization occurs independently of the site of growth, and it is a defining feature of many CRCs.

Characterization of Biosynthetic Cells in CRCs

Recent reports revealed that CRCs expand through the proliferation of tumor cells that are located at the tumor edges in contact with the stroma that surrounds xenografts (van der Heijden et al., 2019; Lenos et al., 2018). In our model systems, however, there were no significant differences in the numbers of Ki67⁺ cells located at the tumor center and in the periphery (Figures S2A–S2D). We confirmed this finding in CRC patient samples (Figures S2E and S2F). The OP-P⁺ and EU⁺ domains only encompassed a fraction of the Ki67⁺ tumor cell population and were similarly distributed in the tumor center and the periphery (Figures 2A and 2B).

Previous studies have shown that a substantial proportion of CRCs exhibited few or no LGR5⁺ cells (Figures 2C and 2D; Merlos-Suárez et al., 2011; Shimokawa et al., 2017). (For convenience, we reproduce in Figure 2E the results from Merlos-Suárez et al.) We investigated how the expression of LGR5 correlated with the rRNA and protein synthesis zonation patterns described above. To this end, we knocked in a tdTomato cassette in the LGR5 locus of patient-derived organoids (PDOs) using a CRISPR-Cas9-based approach that we described elsewhere (Cortina et al., 2017; Figure 2F). In these experiments, we used two different PDOs as model systems: PDO-p18 carries inactivating mutations in APC and functional inactivation of P53 (van de Wetering et al., 2015) and contains a large proportion of LGR5⁺ cells. PDO7 is mutant in four main driver pathways (APC, KRAS, ATM, SMAD4) and represents a model for CRCs with a discrete LGR5⁺ cell population (Table S4). Subsequently, we generated xenografts inoculating these LGR5 reporter PDOs in immunodeficient mice. tdTomato-high cells purified from dissociated xenografts upregulated intestinal stem cell (ISC)-specific genes such as LGR5 and SMOC2, whereas tdTomato[−] cells expressed markers of intestinal

(C) OP-P incorporation in spontaneous liver metastasis generated from intrasplenic (IS) injection of PDO7. Lu, lumen. Scale bars: (C), 5 mm; (C') and (C''), 250 μ m.

(D) EU incorporation in a PDX. Dashed lines outline the epithelial glands. Lu, lumen. Scale bars: (D), 500 μ m; (D'), 250 μ m; (D''), 50 μ m.

(E) Analysis of OP-P and EU in EPHB2 tumor cell populations.

(F) Representative flow cytometry plots of EU and OP-P into EPHB2⁺ or EPHB2[−] tumor cells purified from indicated PDXs.

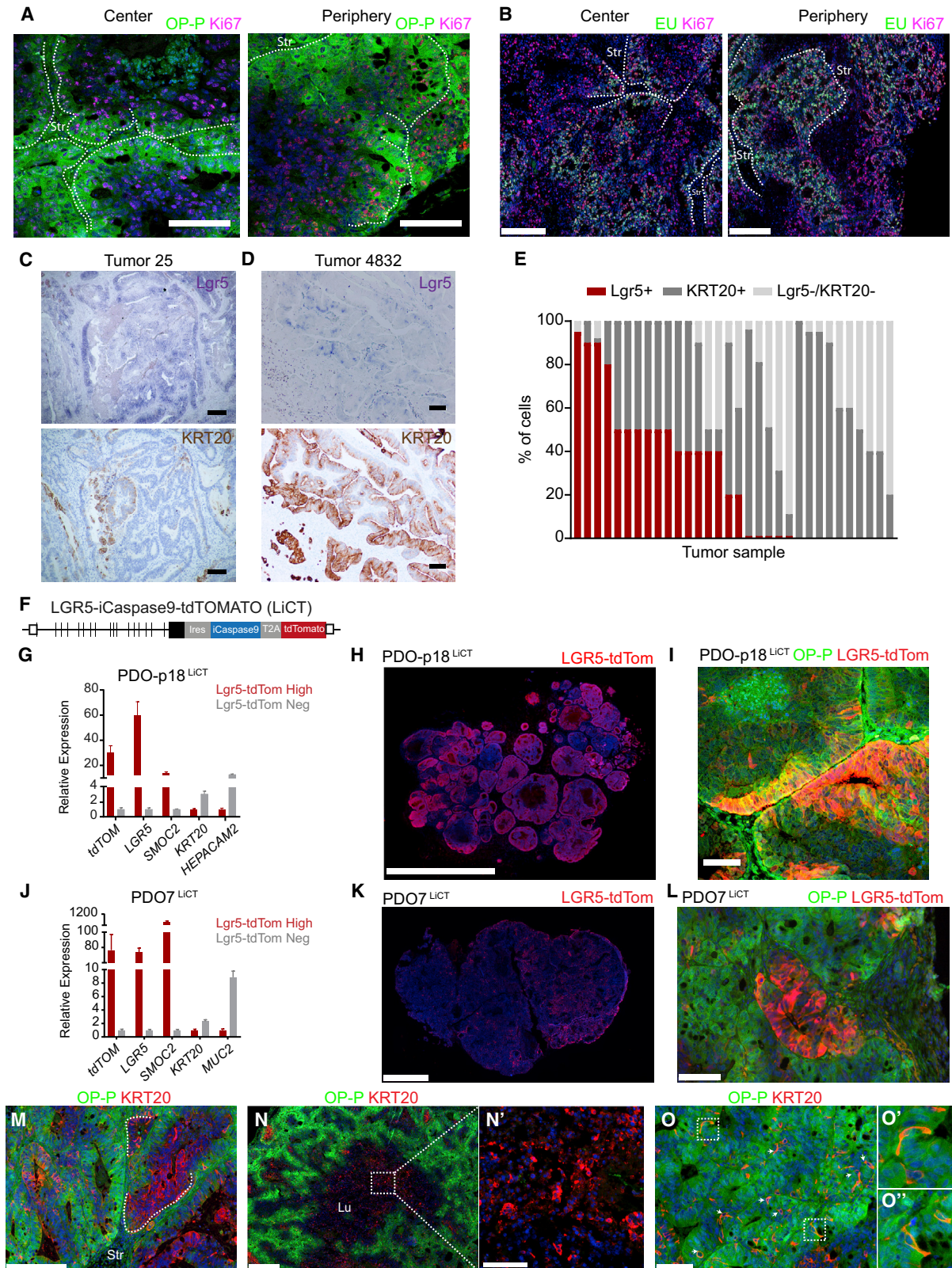
(G) Percentage of OP-P⁺ and EU⁺ cells within EPHB2-high and -low tumor cells. ****p = 1.92×10^{-7} and ****p = 1.51×10^{-9} in a mixed-effects linear model (n = 3 PDX, 2 mice for each PDX).

(H) EPHB2-based cell purification from human CRC samples.

(I) GSEA of EPHB2-high and -low tumor cells sorted from primary CRCs. For all Gene Ontology (GO) SLIM terms, false discovery rate (FDR) q = 0.

(J) Spatial zonation model of protein synthesis-rDNA transcription in CRCs.

Images in (A)–(D) are tiled and stitched.



(legend on next page)

differentiation (Figures 2G and 2J). PDO-p18-derived xenografts contained abundant LGR5⁺ cells (Figure 2H) and we observed overlap between the LGR5⁺ and OP-P⁺ domains in these tumors (Figure 2I). In contrast, PDO7 xenografts exhibited a smaller proportion of LGR5⁺ cells scattered through tumor glands (Figure 2K), most of which were distributed within the OP-P-low/OP-P⁻ domain (Figure 2L).

It was also evident that tumor glands formed by differentiated KRT20⁺ tumor cells did not incorporate OP-P or EU, even if these differentiated cells were immediately adjacent to stroma (examples in Figures 1A–1D and 2M). The lumens of these KRT20⁺ glands often contained dead cells (Figures 2N and 2N'), suggesting that differentiated CRC cells exhibit short lifespans, as previously proposed (Shimokawa et al., 2017). In addition, most CRCs analyzed included a small proportion of KRT20⁺ (0.5%–2%) scattered within the OP-P⁺ domain (Figure 2O, 2O', and 2O''). We conclude that the EU⁺ and OP-P⁺ domains of CRCs are always positioned adjacent to the stroma, yet the stromal localization per se neither defines the biosynthetic capacities of CRC cells nor defines the expression of stem cell differentiation or proliferation marker genes.

Shutdown of rRNA and Protein Synthesis Rates during Tumor Cell Differentiation

Tumor cell differentiation can be enforced in CRC cell lines and organoids through inhibition of WNT signaling (van de Wetering et al., 2002). Expression of a tamoxifen-inducible dominant-negative TCF4 transcription factor in LS174T or SW403 CRC cells triggered the expression of KRT20 and other differentiation markers coinciding with a decline in the levels of ISC genes (Figure 3A). Likewise, mouse intestinal tumoroids engineered to bear activating mutations in Kras (G12D) combined with the loss of function alleles of p53 and a doxycycline-regulated small hairpin RNA (shRNA) targeting Apc (AKP tumoroids) (Dow et al., 2015) undergo differentiation upon the removal of doxycycline leading to the shutdown of β -catenin-TCF4 transcription (Figure 3B). We observed that after prolonged WNT blockade and differentiation (7 days), CRC cell lines and mouse tumoroids exhibited a significant reduction in EU and OP-P incorporation (Figures 3C, 3D, S3A, and S3B). The uptake of methionine analog L-homopropargylglycine (HPG) was also largely reduced (Figures 3E and 3F; text below). In addition, prolonged WNT blockade caused a decrease in pre-rRNA levels (Figure 3G).

The Y10B antibody recognizes mainly cytoplasmic 5.8S rRNA loaded in ribosomes (Lerner et al., 1981; Witte et al., 1991). Using

this antibody, we found that loss of OP-P and EU incorporation coincided with a decrease in the number of assembled ribosomes (Figure 3H). Y10B staining of primary formalin fixed-paraffin embedded (FFPE) patient samples (n = 24) revealed extensive intratumoral heterogeneity in ribosome density. Elevated expression of the pan-differentiation marker KRT20 correlated strongly with lack of 5.8S staining in the vast majority of patients (examples in Figures 3I, 3J, S3C, and S3D). Hence, KRT20⁺ CRC cells not only display a pronounced reduction in rRNA synthesis and protein synthesis rates but also exhibit a reduced number of ribosomes.

To track the production of proteins during cell differentiation, we made use of HPG, which is incorporated into proteins without disturbing their functions (Calve et al., 2016; Dieterich et al., 2010; Signer et al., 2014). CRC cell lines expressed KRT20 protein 4 days after blockade of the WNT pathway (Figure 3L). At this early time point, many KRT20⁺ cells incorporated HPG, implying that during the onset of differentiation protein synthesis rates remain elevated. However, we observed a progressive decline in HPG incorporation during the following 3 days that coincided with the downregulation of rRNA and protein synthesis machinery (Figures 3K and 3L). Pulse-chase experiments revealed that the majority of KRT20 was synthesized during the first 3 days after WNT blockade, yet only limited amounts were produced at a later time point (Figures 3M–3P). Therefore, fully differentiated tumor cells retain long-lived proteins that were synthesized before the protein synthesis machinery was shut down.

Biosynthetic CRC Cells Express Elevated POLR1A Levels

We noticed that prolonged WNT blockade in *in vitro* CRC models caused downregulation of mRNAs encoding for subunits of RNA polymerase I holocomplex, including POLR1A, POLR1B, and POLR1C (Figures 4A and 4B). The rDNA-specific transcription factors TIF-1A and UBTF were also downregulated (Figure 4B). We confirmed a substantial reduction in the major subunit of the RNA polymerase I complex, POLR1A, after 7 days of WNT blockade by western blot (Figure 4C) and immunofluorescence (Figure 4D and S4A). Consistently, KRT20⁺ cells present in xenografts displayed relatively low POLR1A levels (Figures S4B and S4C). The expression of POLR1A was increased in CRC samples compared to normal mucosa, which is consistent with augmented rDNA transcription in tumors (Figure S4D).

To study POLR1A *in vivo*, we used CRISPR-Cas9 technology to knock in an EGFP cassette in frame with the start codon of the

Figure 2. Characterization of Biosynthetic Tumor Cells in CRCs

(A and B) Representative Ki67 and OP-P (A) or EU (B) patterns in PDXs. Dashed lines outline the epithelial glands. Scale bars: (A), 100 μ m; (B), 250 μ m. (C and D) *In situ* hybridization of Lgr5 (top images) and immunohistochemistry (IHC) of KRT20 (bottom images) in serial sections of 2 representative human primary CRCs. Scale bars: 100 μ m. (E) Quantification of Lgr5⁺, KRT20⁺, and double-negative cells across a collection of primary CRC human samples (reproduced from Merlos-Suárez et al., 2011). (F) Schematic representation of the Lgr5-inducible Caspase9-tdTomato (LiCT) targeting construct. (G and J) qRT-PCR analysis of ISC and differentiation genes in PDO-p18-LiCT (G) and PDO7-LiCT (J). Bars depict the mean and upper and lower limits of relative expression obtained from a representative experiment. (H and K) LGR5-tdTomato staining in PDO-p18 (H) and PDO7 (K) tumor xenografts. Scale bars: (H), 2.5 mm; (K), 1 mm. (I and L) LGR5-tdTomato and OP-P staining in PDO-p18 (I) and PDO7 (L) tumor xenografts. Scale bars: (I), 50 μ m; (L), 100 μ m. (M–O) OP-P and KRT20 staining in PDO7 xenografts. In (M), the dashed line delimits a KRT20⁺ gland in contact with the stroma. (N) and (N') show KRT20⁺ cells in the lumen of a tumor gland. (O) Single KRT20⁺ cells intermingled within the OP-P⁺ domain (arrows). Str, stroma; Lu, lumen. Scale bars: (M), 250 μ m; (N), 500 μ m; (O), 100 μ m. The images in (A), (B), (I), and (L)–(O) are tiled and stitched.

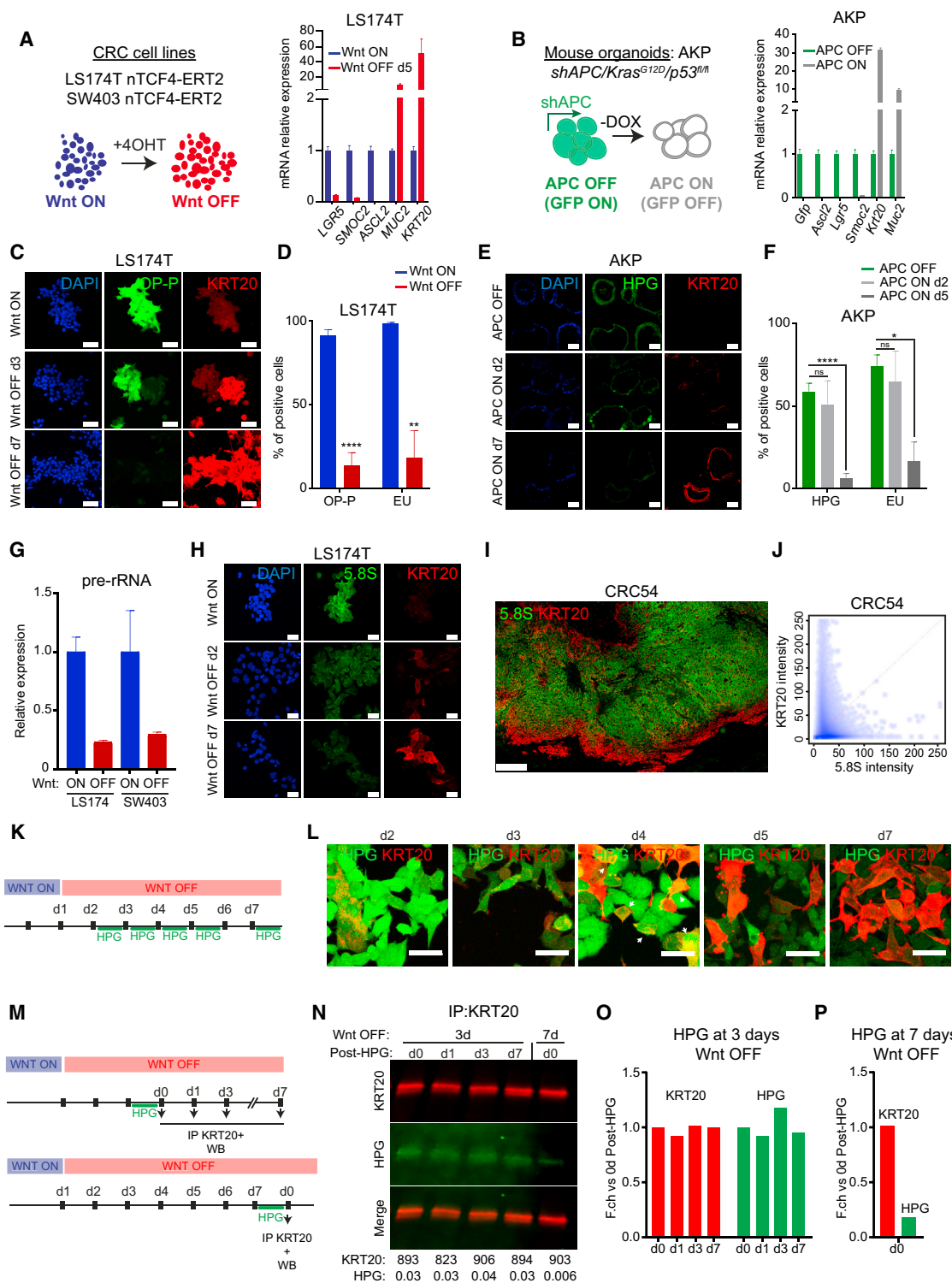


Figure 3. WNT-Driven Differentiation Causes Protein and RNA Synthesis Decrease

(A) qRT-PCR analysis of ISC and differentiation genes in control (Wnt ON) or differentiated (Wnt OFF) LS174T CRC cells. Bars depict the mean and upper and lower limits of relative expression obtained from a representative experiment.
(B) qRT-PCR analysis of ISC and differentiation genes in control (APC OFF) or differentiated (APC ON) AKP mouse organoids. Bars depict the mean and upper and lower limits of relative expression obtained from a representative experiment.
(C) OP-P incorporation and KRT20 in LS174T CRC cells over differentiation. Scale bars: 50 μ m.

(legend continued on next page)

POLR1A gene (Figure 4E). The EGFP-POLR1A fusion protein was located in the nucleolus of knock-in organoids (Figures 4F and S4E). Upon inoculation into immunodeficient mice, PDOs generated xenografts displaying extensive EGFP-POLR1A heterogeneity. EGFP-POLR1A and KRT20⁺ areas were located in mutually exclusive domains in PDXs (Figures 4G and S4F). Isolation of the EGFP-POLR1A-high cell population (brightest 10% tumor cells) from dissociated tumors followed by western blot-confirmed elevated POLR1A levels, whereas their negative counterparts expressed KRT20 (Figures 4H, 4I, S4G, and S4H). EU and OP-P were almost exclusively incorporated in EGFP-POLR1A-high cells purified from both PDO7 and PDO-p18 xenografts (Figures 4J–4N and S4I). Therefore, elevated POLR1A levels characterize the cells that reside within the biosynthetic domains of CRC.

EGFP-POLR1A-high cells purified from xenografts exhibited higher organoid-forming capacity than EGFP-POLR1A-low cells (Figure S4J). Experiments of tumor cell isolation followed by transplantation into secondary recipients revealed that the EGFP-POLR1A-high cell population present in both PDO-p18 and PDO7 was largely enriched in tumor-initiating cells (Figure 4O). Intrasplenic inoculation of tumor cell populations also demonstrated that the vast majority of metastasis-initiating cells reside within the tdTomato-POLR1A-high cell fraction (Figures S4K and S4L).

Characterization of Tumor Cell Heterogeneity by Single-Cell Profiling

We next studied the relationship between stem and differentiated gene programs and the POLR1A-high cell population by single-cell RNA sequencing (scRNA-seq) of PDO7- and PDO-p18-derived xenografts. Unsupervised clustering identified discrete tumor cell populations that we subsequently ascribed to either ISC-like or differentiated-like (absorptive, enteroendocrine, and mucosecreting) phenotypes (Figures 5A, 5F, S5A, and S5B). The LGR5 expression signature labeled ISC-like cells, whereas KRT20 was upregulated in differentiated-like tumor cells (Figures 5B, 5G, S5A, and S5B). These analyses also identified a distinctive population of undifferentiated cells that expressed elevated POLR1A-high signature levels in both xenografts (Figures 5C and 5H). The transcriptomes of the POLR1A-high cell population in both PDO-P18 and PDO7 xenografts were

enriched in gene sets related to proliferation and biosynthetic pathways (Table S7). The two PDO xenografts differed in the expression patterns of the LGR5 signature. Many tumor cells in PDO-p18, including a large fraction of the POLR1A-high cell population, were ISC like and expressed LGR5 (Figures 5B and 5C). In contrast, there was a limited overlap between the POLR1A-high and the LGR5⁺ cell populations in PDO7 (Figures 5G and 5H). Using PDO7-bearing LGR5-tdTomato and POLR1A-EGFP reporter cassettes (Figure S4M), we corroborated that only a minority (10%) of POLR1A-EGFP-high cells were LGR5-tdTomato⁺ cells (Figure S4N). Within the POLR1A-high population, LGR5⁺ and LGR5⁻ cells exhibited differential expression of metabolism-related gene sets (Figures S4O and S4P).

Finally, analysis of gene expression dynamics using pseudotime reconstruction predicted that the origin of the trajectory in both PDO7 and PDO-p18 xenografts corresponded to the POLR1A-high cells, whereas differentiated-like cells were positioned at endpoints (Figures 5D, 5E, 5I, and 5J). Changes in cell states over the pseudotime path were characterized by a progressive decline in POLR1A-high signature expression levels (Figures S5C–S5F).

Clonal Analysis of POLR1A⁺, LGR5⁺, and KRT20⁺ Cells

By means of CRISPR-Cas9, we knocked in lineage-tracing cassettes into the endogenous *POLR1A*, *LGR5*, or *KRT20* locus of PDO7 (Figure 5K). We titrated the amount of tamoxifen necessary to recombine approximately the same number of cells (1%–2%) in the three creERT2 PDO-derived xenografts (Figure S5G). This low recombination frequency facilitated the analysis of the three cell types at the clonal level (Figure 5P). We found no significant differences in the fraction of non-necrotic tumor cells between the three experimental conditions (Figure S5H). The number of clones generated by POLR1A⁺ cells was sustained over time, whereas the frequency of LGR5-derived clones declined at late time points (Figure 5L). In addition, POLR1A⁺ tumor cells produced larger clones (Figures 5M, 5N and 5P) and contributed substantially more cells than LGR5⁺ cells (Figure 5O). Our data also indicated that both POLR1A and LGR5 populations generated progeny that underwent differentiation, as shown by KRT20 labeling (Figure 5Q). Based on these observations, we tentatively conclude that

(D) Percentage of OP-P⁺ and EU⁺ cells detected by flow cytometry in LS174T after 7 days of *in vitro* differentiation. For OP-P, *****p* < 0.0001 (*n* = 4); for EU, ***p* = 0.0078 (*n* = 3) in an unpaired 2-tailed *t* test. Confidence intervals (CIs) are mean ± SEM.

(E) HPG incorporation and KRT20 staining in AKP mouse organoids over differentiation. Scale bars: 50 μm.

(F) Percentage of HPG⁺ and EU⁺ cells detected by flow cytometry in AKP organoids over differentiation. For HPG, *****p* ≤ 0.0001 (*n* = 4); for EU, **p* = 0.0131 (*n* = 3) in an unpaired 2-tailed *t* test. CIs are mean ± SEM.

(G) Pre-rRNA levels in LS174T and SW403 cells after 4 days of differentiation. Bars depict the mean and upper and lower limits of relative expression obtained from a representative experiment.

(H) 5.8S rRNA and KRT20 staining in LS174T cells over differentiation. Scale bars: 20 μm.

(I) Representative 5.8S and KRT20 staining of a primary human CRC sample. Scale bar: 1 mm.

(J) Representative plot of KRT20/5.8S intensity analysis from (I). Kolmogorov-Smirnov (KS) test *p* = 8.35 × 10⁻⁵.

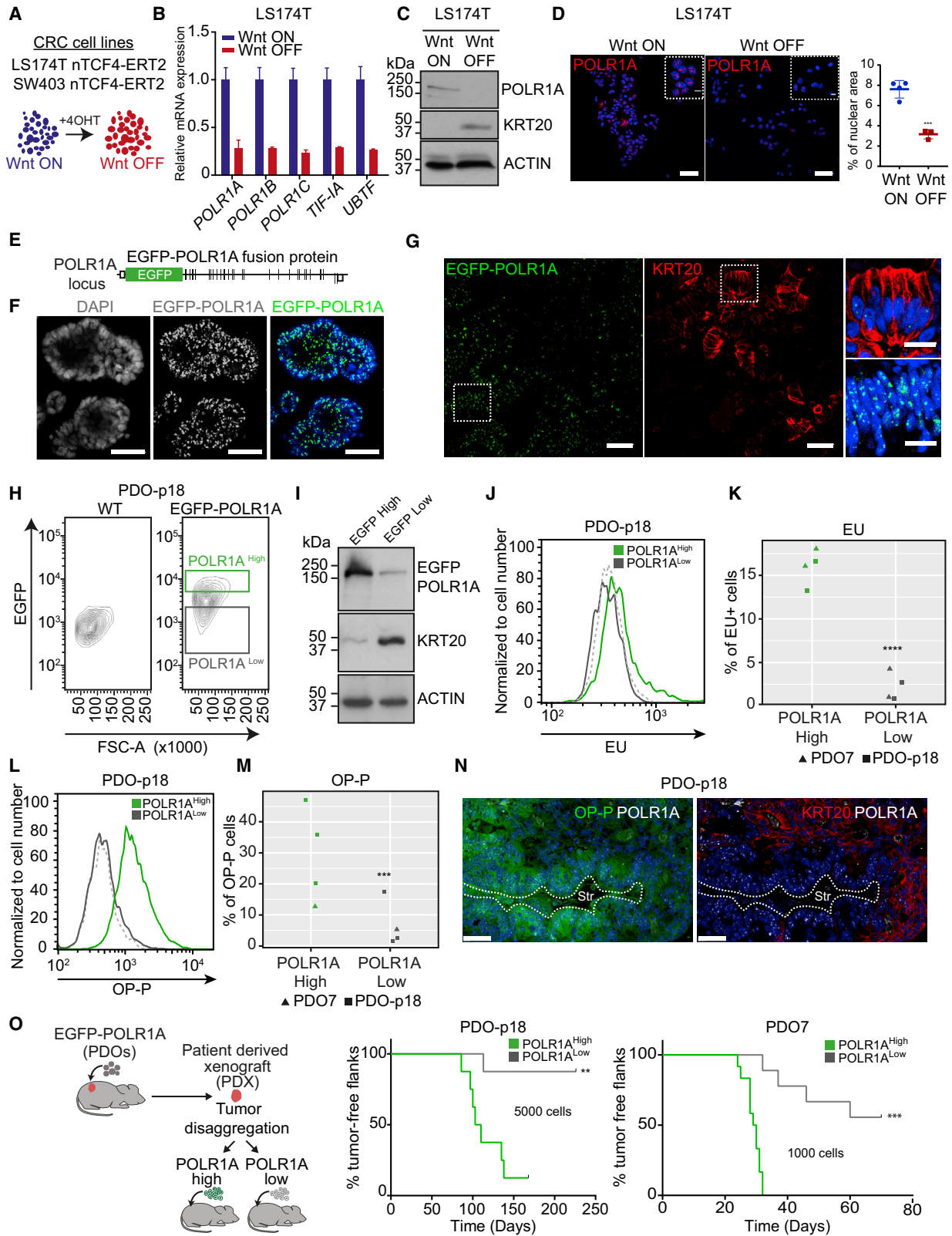
(K) Experimental setup for (L).

(L) HPG incorporation and KRT20 staining in LS174T cells during differentiation. Arrows point at double-positive cells on day 4. Scale bars: 20 μm. Images are tiled and stitched.

(M) Experimental design for protein tracing experiment.

(N) Immunoprecipitation of KRT20 using whole-protein extracts from HPG-labeled and -traced samples. The numbers below the panels indicate the intensity of the signal.

(O and P) Quantification of KRT20 and HPG intensity at day 3 (O) and day 7 (P) of differentiation.



(legend on next page)

POLR1A⁺ biosynthetic cells represent the main population fueling the growth of PDO7 tumors.

Most KRT20⁺ differentiated cells exhibited low proliferative potential and were short-lived (Figures 5L, 5M, and 5O). However, a small proportion of KRT20⁺ cells (2%–5%) generated progeny that expanded over time (Figure 5N), which may indicate that either some cells retained proliferative potential or that a restricted subset of differentiated cells recovered stem cell potential through plasticity. It is, however, important to consider that at the earliest time point of tamoxifen treatment (3 days), only a minority (15%) of tdTomato marked cells represented mature differentiated cells, as shown by lack of expression of KRT20 protein (Figures S5I and S5J). We speculate that due to the decrease in protein synthesis rates, the probability of inducing recombination in terminally differentiated cells is low.

POLR1A-High Cells Are Necessary for Tumor Growth

We next performed experiments of cell ablation using PDOs that carry an inducible caspase 9 (iCasp9) knocked-in either in the *POLR1A* or in the *LGR5* locus (Shimokawa et al., 2017; Figures 6A, 6B, 6J, and 6N). Xenografts derived from inoculation of knock-in PDOs in mice exhibited heterogeneous POLR1A-tdTomato-iCasp9 (POLICT) levels, including KRT20⁺ cells that expressed very low levels of the reporter (Figures 6C and 6D). Analysis of tdTomato by flow cytometry confirmed a wide range of expression, with bright and dim cells differing >25-fold in reporter levels (Figure 6E). POLR1A-tdTomato-high cells expressed higher levels of POLR1A (Figure S6A) and exhibited increased OP-P and EU incorporation compared to POLR1A-tdTomato-low cells (Figures S6C and S6D). Induction of iCasp9 dimerization with AP20187 (Shimokawa et al., 2017) selectively eliminated the brightest POLR1A-tdTomato cells after 5 days (Figure 6E). In addition, we observed an increased frequency of cells expressing low reporter levels, suggesting tumor cell differentiation. By immunofluorescence, we confirmed that only tumor cells expressing the highest Tomato levels were ablated in these experiments (Figure S6B). Upon treatment, the epithelial

compartment, but not the stromal cells of these xenografts, lacked OP-P and EU incorporation (Figures 6G and S6D), demonstrating that we effectively eliminated the cell population that synthesized proteins and rRNA in tumors. Ablation of POLR1A-high cells completely halted the growth of both PDO-p18 and PDO7 xenografts (Figure 6F). It also caused an increase in the number of differentiated cells shown by KRT20 and Alcian blue staining, although this effect was more prominent in PDO7 than in PDO-p18 (Figures 6H, 6I, S6E, and S6F). Genetic ablation of LGR5 cells (Figures 6K, 6O, S6G, and S6H) using an equivalent approach was effective, but only halted growth and OP-P incorporation in PDO-p18 xenografts (Figures 6L and 6M). PDO7 tumors grew steadily and the zonation pattern of protein synthesis was not altered, despite the lack of LGR5⁺ cells (Figures 6P and 6Q). Overall, these results imply that biosynthetic cells labeled by high POLR1A levels sustain tumor growth in both CRCs. The broad expression of LGR5 in PDO-p18, which expands into the POLR1A⁺ compartment, makes this tumor susceptible to LGR5⁺ cell ablation. In contrast, only a minority of LGR5⁺ cells in PDO7 express POLR1A and exhibit biosynthetic capacities, and therefore, the bulk of the LGR5⁺ cell population is dispensable for tumor growth.

Therapeutic Targeting of Biosynthetic Tumor Cells

Treatment of xenografts with FOLFIRI, a chemotherapeutic commonly used in CRC patients, slowed down tumor growth and reduced the number of POLR1A-tdTomato-high cells (Figures S6I–S6K). The incorporation of OP-P⁺ was also diminished (Figure S6L). Concomitantly, FOLFIRI-treated xenografts exhibited an increased abundance of POLR1A-tdTomato-Low cells (Figure S6K) and contained substantially more KRT20⁺ cells at experimental endpoints (Figures S6L and S6M). Therefore, FOLFIRI treatment reproduced to some extent the effects of genetic ablation of POLR1A-high cells, although it failed to completely eliminate the tumor biosynthetic compartments.

BMH-21 is a small molecule that induces the degradation of POLR1A (Peltonen et al., 2014). *In vitro* treatment with BMH-21

Figure 4. POLR1A-High Tumor Cells Display High Biosynthetic and Tumorigenic Capacities

- (A) CRC cell line differentiation via inducible NTCF4.
(B) qRT-PCR of rRNA transcriptional machinery components in LS174T after 4 days of *in vitro* differentiation. Bars depict the mean and upper and lower limits of relative expression obtained from a representative experiment.
(C) Western blot analysis of POLR1A and KRT20 in LS174T during differentiation.
(D) POLR1A staining in LS174T tumor cells after 7 days of *in vitro* differentiation. Scale bars: 20 μ m. Right panel: quantification of nuclear area occupied by POLR1A in control (Wnt ON) or upon differentiation (Wnt OFF). $p = 0.0005$ in unpaired 2-tailed t test ($n = 4$ images for Wnt ON and $n = 3$ images for Wnt OFF). CIs are mean \pm SEM.
(E) Knock-in construct for the generation of EGFP-POLR1A fusion protein.
(F) EGFP-POLR1A labels the nucleoli of PDO-p18 *in vitro*. Scale bar: 50 μ m.
(G) EGFP-POLR1A and KRT20 staining in PDO-p18 xenografts. Scale bars: 50 μ m, and 10 μ m in the insets.
(H) Representative flow cytometry plot of EGFP-POLR1A in knock-in PDO-p18 xenografts (right plot). Squares indicate the sorted EGFP-POLR1A populations. The top 10% were considered to be POLR1A-high.
(I) Western blot of POLR1A and KRT20 in indicated sorted populations from (H).
(J) Representative flow cytometry plot of EU incorporation in EGFP-POLR1A cells purified from PDO-p18 xenografts.
(K) Percentage of EU⁺ cells in POLR1A sorted cells from tumor xenografts. **** $p < 0.0001$ in a mixed-effects linear model ($n = 2$ different PDX and 2 experimental replicates).
(L) Representative flow cytometry plot of OP-P incorporation in EGFP-POLR1A tumor cell populations purified from PDO-p18 xenograft.
(M) Percentage of OP-P⁺ cells in POLR1A sorted cells from tumor xenografts. *** $p = 0.001$ in a mixed-effects linear model ($n = 2$ different PDX; 3 replicates for PDO-p18 and 1 for PDO7).
(N) OP-P and POLR1A (left panel) and KRT20 and POLR1A (right panel) staining in PDO-p18 xenograft. Scale bar: 50 μ m.
(O) Tumor initiation capacity of EGFP-POLR1A-high and -low tumor cells purified from PDO-p18 (left) and PDO7 (right). Kaplan-Meier plots ($n = 8$ xenografts). ** $p = 0.0032$ for PDO-p18 and **** $p < 0.0001$ for PDO7 in a Gehan-Breslow-Wilcoxon test.

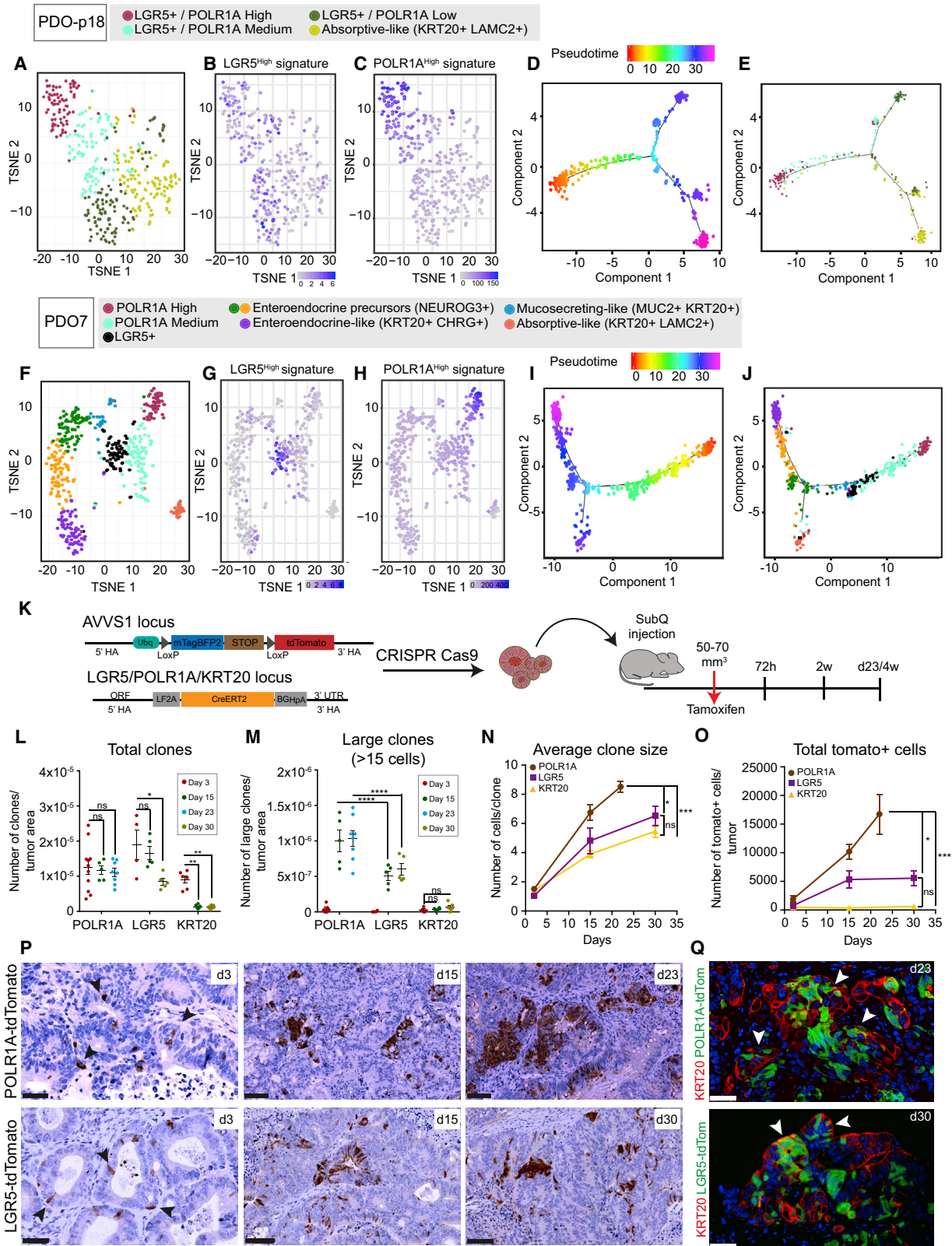


Figure 5. Mapping of Tumor Cell Populations by Single-Cell Profiling and Clonal Analysis

(A and F) t-distributed Stochastic Neighbor Embedding (t-SNE) plots of 388 (PDO-p18, A) and 511 (PDO7, F) single cells from tumor xenografts colored by cluster identities.

(legend continued on next page)

downregulated POLR1A levels and induced overt differentiation of PDO7 (Figures S6N–S6P). We observed similar, yet milder effects in xenografts (Figures S6Q and S6R). Higher BMH-21 doses resulted in mouse toxicity, which limited its therapeutic efficacy in the *in vivo* setting.

Irreversible Phenotype of KRT20⁺ CRC Cells

Experiments of POLR1A-high cell ablation over 10 days followed by a long recovery period in the absence of dimerizer revealed that growth remained continuously halted (Figures 7A and 7B). Analysis of the remaining tumor mass 7 days after stopping dimerizer treatment showed the presence of KRT20⁺ tumor cells in direct contact with the stroma that exhibited largely reduced protein synthesis rates (Figure 7C). After extended periods of time (>25–30 days), tumors slowly reinitiated growth. This was likely due to residual cells that acquired resistance to iCasp9 ablation, as inferred by the fact that tumors continuously treated with dimerizer expanded with almost identical kinetics (data not shown) and that organoids established from samples taken at the onset of the re-growth phase were resistant to dimerizer treatment *in vitro* (Figures S7A and S7B).

To explore further the irreversibility of the differentiated state, we made use of AKP tumoroids bearing a doxycycline-regulated *shApc* cassette (Figure 7D). Tumoroids forced to differentiate *in vitro* during 2 days in the absence of doxycycline (APC ON) that were subsequently cultured for 7 days with doxycycline (APC OFF) partially retained rRNA transcription, protein synthesis, and growth rates (Figures 7E–7G). Therefore, the loss of biosynthetic capacity due to short-term differentiation (2 days) is reversible to some extent. In contrast, switching to doxycycline media after 5 days of differentiation did not restore growth (Figures 7G and S7D), despite re-expression of the GFP-*Apc* shRNA cassette (Figure S7C). Most cells in these tumoroids were KRT20⁺ (Figure 7H) and exhibited a reduced capacity to synthesize rRNA or proteins, even after prolonged culturing in doxycycline-supplemented media (i.e., 7 days) (Figures 7E and 7F). Consistent with this finding, AKP tumoroids did not recover POLR1A levels after long-term (7 days) differentiation (Figures 7H and 7I). Transcriptomic profiling of mouse tumoroids at early (2 days of *Apc* restoration) versus late-stage differentiation (7 days of *Apc* restoration) revealed that downregulation of

gene sets related to biosynthesis such as ribosome, nucleolus, ribonucleoprotein assembly, and ribosome biogenesis occurred only 7 days after restoring APC, concordant with the time frame of irreversible differentiation (Figures S7F and S7G).

To study reversibility *in vivo*, we generated xenografts by inoculating AKP tumoroids in mice (Figure 7J). Removal of doxycycline halted tumor growth, upregulated the expression of KRT20, and reduced EU and HPG incorporation in xenografts (Figures 7K, 7L, and S7E). This phenomenon was partially reversible by doxycycline supplementation after 8 days, including the restoration of HPG and EU incorporation. However, 20 days after continuous APC expression, addition of doxycycline did not rescue tumor growth, rRNA, or protein synthesis rates (Figures 7K, 7L, and S7E). The remaining tumor mass was composed mostly of KRT20⁺ cells directly in contact with the tumor stroma. POLR1A levels remained downregulated at this later time point (Figure 7M). Therefore, prolonged differentiation causes permanent downregulation of the biosynthetic capacities of CRC cells (Figure 7N).

DISCUSSION

Homeostasis of adult tissues requires controlled protein synthesis rates, and distinct cell types in healthy tissues, including stem cells and their differentiated progeny, exhibit different biosynthetic capabilities (Blanco et al., 2016; Signer et al., 2014). In tumors, this regulation is disrupted by oncogenic alterations, many of which enhance the cell biosynthetic machinery, including rDNA transcription, ribosomal biogenesis, and protein production rates (Bustelo and Dosil, 2018; Pelletier et al., 2018; Ruggero, 2012). Genetic manipulations leading to diminished ribosomal function and protein production exert robust anti-tumorigenic effects (Ajore et al., 2017; Barna et al., 2008; Peltonen et al., 2014; Signer et al., 2014). Notwithstanding the high biosynthetic requirements of cancers, our data evidence a progressive loss of biosynthetic activity due to the pervasive differentiation that tumor cells experience in CRCs. Fittingly, in models of WNT-dependent pancreatic cancer, inhibition of WNT signaling using Porcupine inhibitors causes differentiation (Jiang et al., 2013), and this process is accompanied by downregulation of POLR1A, POLR1B, and other genes involved in

(B, C, G, and H) Normalized expression of the LGR5 (B and G) and the POLR1A-high (C and H) signatures in PDO-p18 (B and C) and PDO7 (G and H).

(D, E, I, and J) Trajectory graph representations for PDO-p18 (D and E) and PDO7 (I and J), color-coded by pseudotime ordering of cells (D and I) and their cluster identity (E and J).

(K) Knock-in constructs and experimental design for lineage tracing experiments.

(L) Quantification of total number of clones per tumor area at indicated time points. Each dot represents quantifications in a section of a different tumor. $n = 4–10$ tumors per time point and cell population. * $p = 0.0107$ and ** $p < 0.002$ in a 2-way ANOVA using Tukey's multiple comparison test. CIs are mean \pm SEM.

(M) Quantification of the number of large clones (>15 cells) per tumor area at indicated time points. Each dot represents quantifications in a section of a different tumor. $n = 4–10$ tumors per time point and population. **** $p < 0.0001$ in a 2-way ANOVA using Tukey's multiple comparison test. CIs are mean \pm SEM.

(N) Quantification of clone size over time. Data represent the average number of cells per clone. Each dot represents quantifications in a section of a different tumor. $n = 4–10$ tumors per time point and population. * $p = 0.026$ and *** $p = 0.005$ in a 1-way ANOVA using Tukey's multiple comparison test for the last time points. CIs are mean \pm SEM.

(O) Quantification of the total number of tomato⁺ cells per tumor sample over time. Data represent the average of tomato⁺ cells per time point. Each dot represents quantifications in a section of a different tumor. $n = 4–10$ tumors per time point and population. * $p = 0.035$ and *** $p = 0.007$ in a 1-way ANOVA using Tukey's multiple comparison test for the last time points. CIs are mean \pm SEM.

(P) Representative images of tdTomato on tumor xenografts. Arrowheads point to single-cell clones induced at day 3. Scale bars: 50 μm in d3 and 100 μm in d15 and d23 and d30.

(Q) Immunofluorescence (IF) for KRT20 and tdTomato in tumor sections after 23 or 30 days of tamoxifen treatment. White arrowheads indicate tdTomato clones containing KRT20⁺ cells. Scale bars: 50 μm . Images are tiled and stitched.

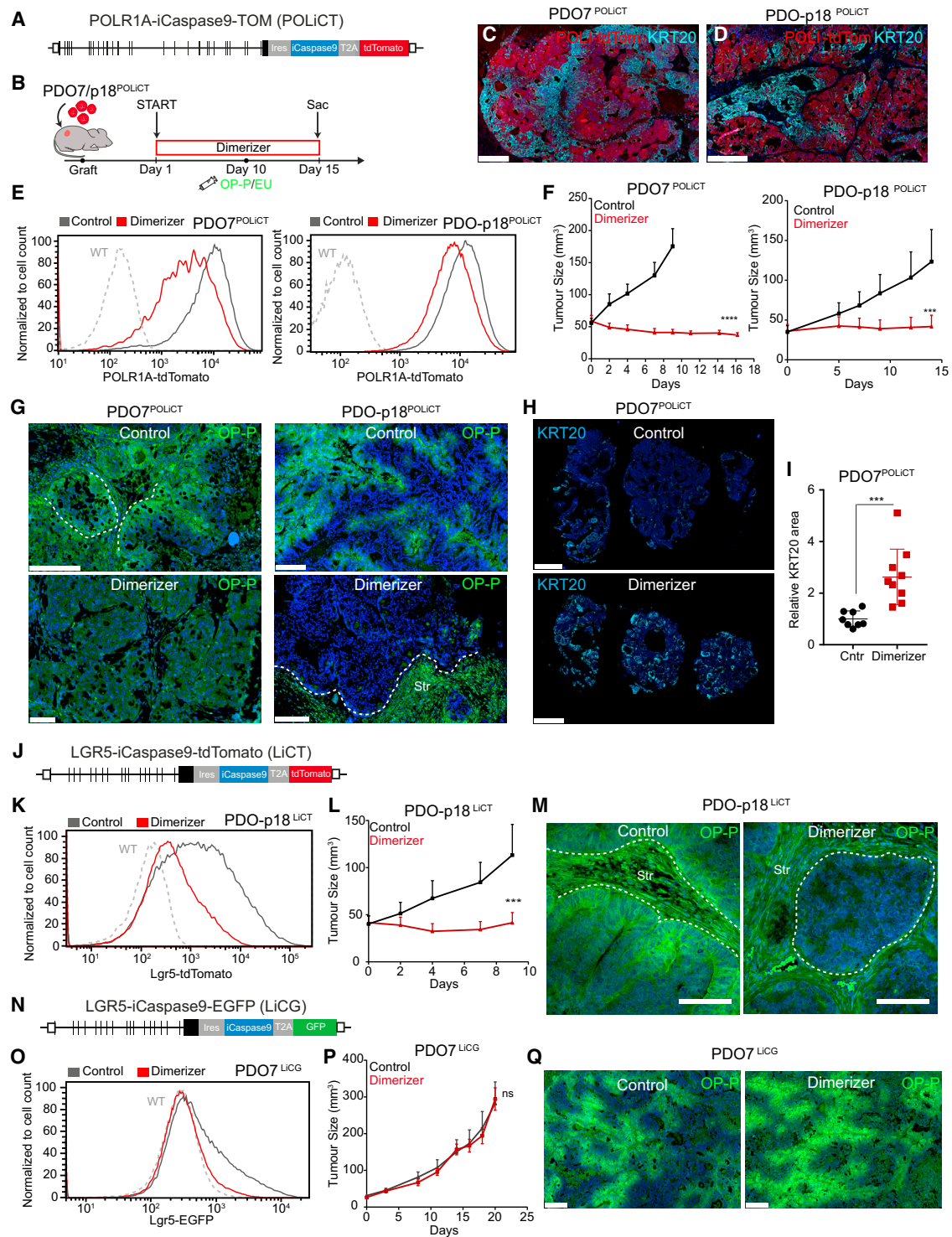


Figure 6. POLR1A-High Tumor Cells Sustain CRC Growth

(A) POLR1A knock-in cell ablation cassette (POLiCT) in PDOs.

(B) Experimental design of *in vivo* ablation experiments.

(C and D) Representative images of tdTomato and KRT20 in xenografts from POLiCT knock-in PDOs. Scale bars: 250 μ m.

(E) Representative flow cytometry plots of tdTomato expression in controls or 4 days post-POLR1A ablation in PDO7 (left) and PDO-p18 (right) *in vivo*. Wild-type (WT) unmodified clones are shown for reference.

(F) Tumor growth during chronic POLR1A ablation. **** $p < 0.0001$ and *** $p = 0.004$ in a 2-tailed t test. For PDO7, $n = 3$ control and $n = 6$ treated tumors. For PDO-p18, $n = 5$ control and $n = 6$ treated tumors. Cls are mean \pm SEM.

(legend continued on next page)

ribosomal biogenesis (Madan et al., 2018). It is well established that signaling pathways that promote biosynthesis such as mammalian target of rapamycin (mTOR) enhance cap-dependent translation, whereas stress conditions, including nutrient deprivation or hypoxia, can activate alternative modes of translation, for example, via internal ribosome entry sites (Robichaud and Sonenberg, 2017; Robichaud et al., 2019). Thus, the vastly reduced protein synthesis rates present in terminally differentiated cells may still be sufficient to translate specific mRNAs. Likewise, the high protein synthesis rates shown by POLR1A-high cells may favor the translation of RNA subsets important for the biology of cancer stem cells.

Many CRCs contain abundant LGR5⁺ cells, yet lineage-tracing analysis suggests that only a small proportion of them function as CSCs (Kozar et al., 2013). Our results support this conclusion. Other CRCs contain few to no LGR5⁺ cells (Merlos-Suárez et al., 2011; Shimokawa et al., 2017), but may still exhibit a hierarchical organization. The same caveats could be applied to other putative stem cell marker genes. In addition, LGR5⁻ cells present in primary CRCs act as seeds for metastasis in experimental models (Fumagalli et al., 2020). Our study defines functionally the CSC population in CRC: we propose that CSCs represent a subset of tumor cells with elevated rDNA transcription rates and a protein synthesis capacity dedicated to fuel tumor growth. We show that both LGR5⁺ and LGR5⁻ tumor cells that display elevated biosynthetic features function as CSCs in transplantation experiments and in intact tumors. The finding that the biosynthetic cell population occupies a basal position within the tumor glands suggests a role for the underlying mesenchymal cells in instructing their phenotype. However, proximity to this niche does not define unequivocally an elevated biosynthetic capacity, as many CRCs contain KRT20⁺ and LGR5⁺ cells in direct contact with the stroma that nevertheless exhibit low protein and rRNA synthesis rates. Our findings fit well with a model whereby the properties of cancer cells are defined both by the microenvironment and cell-intrinsic programs dictated by a stem cell hierarchy.

Previous experiments of KRT20⁺ tumor cell fate mapping have shown that this cell population gives rise mostly to short-lived progeny but can revert to an LGR5⁺ state upon ablation of this CSC pool (Shimokawa et al., 2017). It is, however, important to consider that at the onset of differentiation, CRC cells incorporate elevated OP-P and EU levels. We speculate that these early differentiated cells exhibit a plastic phenotype and can return to a CSC state if necessary. Nevertheless, our findings imply that as

differentiation progresses, the capacity of differentiated cells to revert their state becomes gradually limited due to the downregulation of the rDNA transcription machinery. In a subset of CRCs, continuous ablation of biosynthetic CSCs exhausts the progenitor cell pool and causes irreversible tumor cell differentiation, an observation that may inspire the design of effective anti-CSC therapies.

STAR★METHODS

Detailed methods are provided in the online version of this paper and include the following:

- KEY RESOURCES TABLE
- RESOURCE AVAILABILITY
 - Lead Contact
 - Materials Availability
 - Data and Code Availability
- EXPERIMENTAL MODEL AND SUBJECT DETAILS
 - Mouse strains and tumor cell injections
 - *In vivo* treatments
 - Orthotopic models and primary CRC samples
 - Organoid *in vitro* culture
 - N-TCF4 expressing CRC cells lines
- METHOD DETAILS
 - Organoid formation experiments
 - Immunostaining and confocal imaging
 - Histology and tissue stainings
 - Histological Image Acquisition
 - sgRNA design
 - Donor plasmid construction
 - Generation of CRISPR-Cas9 knock-in PDOs
 - Genotyping PCR and Southern blot
 - RNA extraction and quantitative RT-qPCR
 - Protein extraction and western blot analysis
 - *In vitro* click chemistry, in-gel fluorescence, IP
 - Analysis of protein and RNA synthesis by flow cytometry and microscopy
 - Xenografts disaggregation and cell isolation
 - Generation of POLR1A and LGR5 signatures
 - Microarrays
 - Cell sorting and libraries preparation for Single-cell RNA-seq
- QUANTIFICATION AND STATISTICAL ANALYSES
 - General quantifications

(G) OP-P incorporation in control tumors or after 10 days of POLR1A ablation. Str, stroma. Dashed lines delimit tumor glands from stroma. Scale bars: 250 and 100 μ m.

(H) KRT20 staining in control or POLR1A-ablated PDO7. Scale bars: 2.5 mm.

(I) Quantification of KRT20⁺ areas in control or POLR1A-ablated PDO7 tumors. ***p = 0.0009 in an unpaired 2-tailed t test. n = 8 controls and n = 9 treated tumors. CIs are mean \pm SEM.

(J) Knock-in ablation cassette for the generation of LiCT.

(K) Representative flow cytometry plot of LGR5-tdTomato levels in control or after 5 days of dimerizer in PDO-p18.

(L) Tumor growth during chronic ablation of LGR5⁺ tumor cells in PDO-p18. ***p = 0.0010.

(M) OP-P patterns in untreated mice or after 14 days of dimerizer. Dashed lines delimit the tumor glands. Scale bars: 250 μ m. Str: stroma.

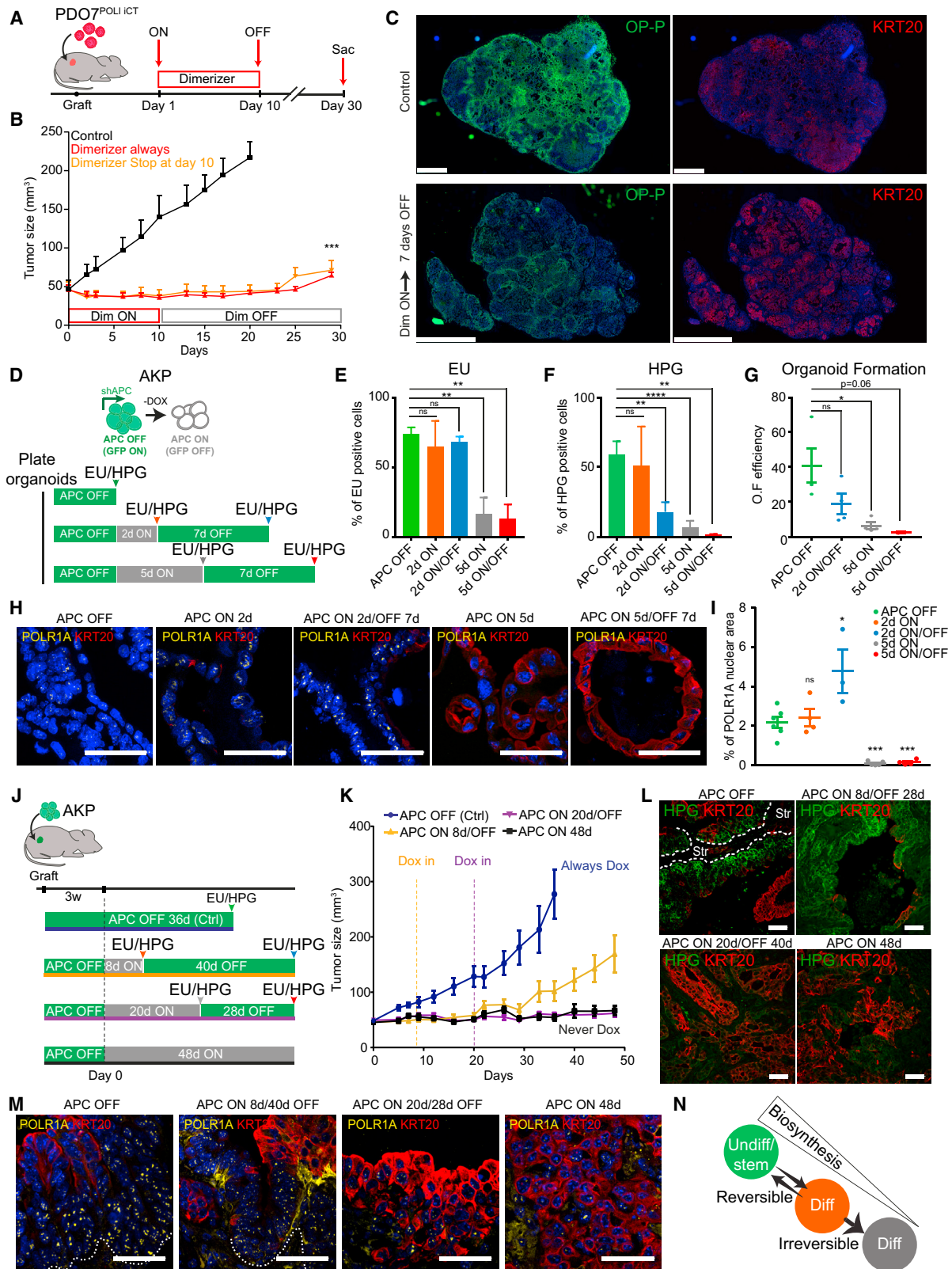
(N) Knock-in ablation cassette for the generation of LGR5-iCaspase9-EGFP (LiCG) in PDO7.

(O) Representative flow cytometry plot of LGR5-EGFP in control conditions or after 5 days of dimerizer in PDO7.

(P) Tumor growth during chronic ablation of LGR5 tumor cells in PDO7.

(Q) OP-P patterns in untreated mice or after 14 days of dimerizer. Scale bars: 250 μ m.

Images in (C) and (D) are tiled and stitched.



(legend on next page)

- Clonal quantification for *in vivo* lineage tracing
- POLR1A expression analysis in colon samples from human cohort
- Microarray analyses
- RNA-Seq data
- Single-cell RNA-seq data analysis
- Single-cell RNA-Seq data – enrichment analysis
- Statistical analyses
- Sample sizing and collection

SUPPLEMENTAL INFORMATION

Supplemental Information can be found online at <https://doi.org/10.1016/j.stem.2020.04.012>.

ACKNOWLEDGMENTS

We thank all of the members of the Battle lab and IRB Barcelona core facilities for histopathology, genomics, mouse mutant, and microscopy, as well as the flow cytometry for extensive support; Raúl Méndez for advice; Antonio Berenguer and Camille Stephan-Otto Attolini for statistical analyses; Giorgio Stassi and the Hubrecht Organoid Technology (HUB, The Netherlands) for sharing PDO7 and PDO-p18, respectively; and Institut d'Investigacions Biomèdiques August Pi i Sunyer (IDIBAPS, Spain) and Hospital del Mar Biobanks for samples. C. Morral and A.A. held La Caixa (Spain) predoctoral fellowships and J.S. held Juan de la Cierva (Spain) postdoctoral fellowship from the Ministerio de Economía y Competitividad (MINECO, Spain; SAF2017-89109-P). H.H. is a Miguel Servet (CP14/00229) researcher funded by Instituto de Salud Carlos III (ISCIII, Spain), Agencia Estatal de Investigación (AEI, Spain) and Fondo Europeo de Desarrollo Regional (FEDER, European Union). C. Moutinho is a postdoctoral fellow of the Asociación Española Contra el Cáncer (AECC, Spain). This work has been supported by grants from the European Research Council (ERC AdvG 340176), the WorldWide Cancer Research (WWCR, European Union; Grant 12_1209), and Agència de Gestió d'Ajuts Universitaris i de Recerca (AGAUR, Spain; 2017 SGR 698) to E.B., and by Fondo de Investigaciones Sanitarias (FIS, Spain; P116-01898) to A.V.

AUTHOR CONTRIBUTIONS

E.B. supervised the study. E.B., C. Morral, and J.S. wrote the manuscript. C. Morral analyzed the biosynthetic cells in tissues and the EPHB2* tumor cells, generated knock-in PDOs, performed the experiments of cell ablation, tested the effects of chemotherapy, and performed the lineage-tracing experiments. J.S. analyzed the effects of WNT blockade and analyzed 5.8S in the tumor samples. X.H.-M. performed the xenograft experiments. C.C. and F.S. per-

formed the LGR5 ablation experiments. D.S. helped screen the KI organoids. A.A. helped in the KRT20 quantification and clonal analysis. G.T. generated the LGR5 and KRT20 lineage-tracing organoids. M.S. and A.C.-M. performed the immunohistochemistry (IHC). G.W. generated the NTCF4 cell lines. A.M.-S. quantified the *Lgr5* and KRT20 in situ hybridization (ISH) and immunohistochemistry (IHC) in patient samples. E.S. provided logistic support. E.M., C. Moutinho, and H.H. performed the scRNaseq experiments. S.W.L. and L.E.D. generated the AKP tumoroids.

DECLARATION OF INTERESTS

The authors declare no competing financial interests.

Received: July 4, 2019

Revised: February 20, 2020

Accepted: April 19, 2020

Published: May 11, 2020

REFERENCES

- Ajore, R., Raiser, D., McConkey, M., Jöud, M., Boidol, B., Mar, B., Saksena, G., Weinstock, D.M., Armstrong, S., Ellis, S.R., et al. (2017). Deletion of ribosomal protein genes is a common vulnerability in human cancer, especially in concert with *TP53* mutations. *EMBO Mol. Med.* **9**, 498–507.
- Ashburner, M., Ball, C.A., Blake, J.A., Botstein, D., Butler, H., Cherry, J.M., Davis, A.P., Dolinski, K., Dwight, S.S., Eppig, J.T., et al.; The Gene Ontology Consortium (2000). Gene ontology: tool for the unification of biology. *Nat. Genet.* **25**, 25–29.
- Aytes, A., Molleví, D.G., Martínez-Iniesta, M., Nadal, M., Vidal, A., Morales, A., Salazar, R., Capellà, G., and Villanueva, A. (2012). Stromal interaction molecule 2 (STIM2) is frequently overexpressed in colorectal tumors and confers a tumor cell growth suppressor phenotype. *Mol. Carcinog.* **51**, 746–753.
- Barna, M., Pusic, A., Zollo, O., Costa, M., Kondrashov, N., Rego, E., Rao, P.H., and Ruggero, D. (2008). Suppression of Myc oncogenic activity by ribosomal protein haploinsufficiency. *Nature* **456**, 971–975.
- Bates, D., Mächler, M., Bolker, B., and Walker, S. (2014). Fitting Linear Mixed-Effects Models using lme4. *J. Stat. Softw.* **67**, <https://doi.org/10.18637/jss.v067.i01>.
- Battle, E., Henderson, J.T., Beghtel, H., van den Born, M.M.W., Sancho, E., Huls, G., Meeldijk, J., Robertson, J., van de Wetering, M., Pawson, T., and Clevers, H. (2002). Beta-catenin and TCF mediate cell positioning in the intestinal epithelium by controlling the expression of EphB/ephrinB. *Cell* **111**, 251–263.
- Blanco, S., Bandiera, R., Popis, M., Hussain, S., Lombard, P., Aleksic, J., Sajini, A., Tanna, H., Cortés-Garrido, R., Gkatza, N., et al. (2016). Stem cell

Figure 7. Loss of Biosynthetic Capacity Drives CRCs into an Irreversible Differentiation State

- (A) Experimental design.
- (B) Tumor growth in untreated mice, during permanent dimerizer treatment (in red), or after 10 days of dimerizer treatment (in yellow) to ablate POLR1A in PDO7. ***p = 0.0010 and **p = 0.0008 in an unpaired 2-tailed t test (n = 3 control, n = 6 always dimerizer, n = 6 stop dimerizer tumors). Cls are mean ± SEM.
- (C) OP-P incorporation and KRT20 expression in control tumors or in tumors 7 days after dimerizer withdrawal. Scale bars: 1 mm (upper images) and 2.5 mm (lower images).
- (D) Experimental design for *in vitro* reversibility experiments in AKP organoids. Arrows indicate sample collection.
- (E and F) Quantification of EU (E) or (F) HPG incorporation during differentiation (ON) and after reversion (ON/OFF). For EU: p = 0.6, p = 0.5, **p = 0.004, and **p = 0.0019 (n = 4, 3, 2, 3, 3); and HPG: p = 0.62, **p = 0.007, ****p < 0.0001, and **p = 0.0015 (n = 4, 4, 2, 4, 2) in an unpaired 2-tailed t test. Cls are mean ± SEM.
- (G) Organoid formation assay during *in vitro* differentiation (ON) and after reversion (ON/OFF). p = 0.10, *p = 0.01, p = 0.06 (n = 4, 4, 4, 2) in an unpaired 2-tailed t test. Cls are mean ± SEM.
- (H) Representative examples of POLR1A and KRT20 staining in organoids during *in vitro* differentiation (ON) or after reversion (ON/OFF). Scale bars: 50 μm.
- (I) Quantification of POLR1A nuclear area from (H). p = 0.6, *p = 0.01, ***p = 0.0001, and ***p = 0.0006 (n = 6, 4, 3, 5 images per condition) in an unpaired 2-tailed t test. Cls are mean ± SEM.
- (J) Experimental design for *in vivo* reversibility experiments of AKP tumors.
- (K) Tumor growth corresponding to (J). **p = 0.0088 and p = 0.709 in an unpaired 2-tailed t test (n = 8, 10, 7 tumors). Cls are mean ± SEM.
- (L) Representative images of HPG incorporation and KRT20 in AKP tumor xenografts.
- (M) POLR1A and KRT20 in AKP xenografts during differentiation (ON) and after the reversion (ON/OFF). Scale bars: 50 μm.
- (N) Differentiation-driven irreversible loss of plasticity in CRC. Images in (H), (L), and (M) are tiled and stitched.

- function and stress response are controlled by protein synthesis. *Nature* **534**, 335–340.
- Bolstad, B.M., Collin, F., Brettschneider, J., Simpson, K., Cope, L., Irizarry, R.A., and Speed, T.P. (2005). Quality Assessment of Affymetrix GeneChip Data. In *Bioinformatics and Computational Biology Solutions Using R and Bioconductor*, R. Gentleman, V. Carey, W. Huber, R. Irizarry, and S. Dudoit, eds. (Springer), pp. 33–47.
- Bunn, A., and Korpela, M. (2014). Crossdating in *dpIR*. <https://mran.microsoft.com/snapshot/2014-11-17/web/packages/dpIR/vignettes/xdate-dpIR.pdf>.
- Bustelo, X.R., and Dosl, M. (2018). Ribosome biogenesis and cancer: basic and translational challenges. *Curr. Opin. Genet. Dev.* **48**, 22–29.
- Calon, A., Espinet, E., Palomo-Ponce, S., Tauriello, D.V.F., Iglesias, M., Céspedes, M.V., Sevillano, M., Nadal, C., Jung, P., Zhang, X.H.F., et al. (2012). Dependency of colorectal cancer on a TGF- β -driven program in stromal cells for metastasis initiation. *Cancer Cell* **22**, 571–584.
- Calve, S., Witten, A.J., Ocken, A.R., and Kinzer-Ursem, T.L. (2016). Incorporation of non-canonical amino acids into the developing murine proteome. *Sci. Rep.* **6**, 32377.
- Cortina, C., Turon, G., Stork, D., Hernando-Momblona, X., Sevillano, M., Aguilera, M., Tosi, S., Merlos-Suárez, A., Stephan-Otto Attolini, C., Sancho, E., and Batlle, E. (2017). A genome editing approach to study cancer stem cells in human tumors. *EMBO Mol. Med.* **9**, 869–879.
- Dalerba, P., Dylla, S.J., Park, I.K., Liu, R., Wang, X., Cho, R.W., Hoey, T., Gurney, A., Huang, E.H., Simeone, D.M., et al. (2007). Phenotypic characterization of human colorectal cancer stem cells. *Proc. Natl. Acad. Sci. USA* **104**, 10158–10163.
- Dalerba, P., Kalisky, T., Sahoo, D., Rajendran, P.S., Rothenberg, M.E., Leyrat, A.A., Sim, S., Okamoto, J., Johnston, D.M., Qian, D., et al. (2011). Single-cell dissection of transcriptional heterogeneity in human colon tumors. *Nat. Biotechnol.* **29**, 1120–1127.
- de Sousa e Melo, F., Kurtova, A.V., Harnoss, J.M., Kljavin, N., Hoeck, J.D., Hung, J., Anderson, J.E., Storm, E.E., Modrusan, Z., Koeppen, H., et al. (2017). A distinct role for *Lgr5*⁺ stem cells in primary and metastatic colon cancer. *Nature* **543**, 676–680.
- Dieterich, D.C., Hodas, J.J.L., Gouzer, G., Shadrin, I.Y., Ngo, J.T., Triller, A., Tirrell, D.A., and Schuman, E.M. (2010). In situ visualization and dynamics of newly synthesized proteins in rat hippocampal neurons. *Nat. Neurosci.* **13**, 897–905.
- Dobin, A., Davis, C.A., Schlesinger, F., Drenkow, J., Zaleski, C., Jha, S., Batut, P., Chaisson, M., and Gingeras, T.R. (2013). STAR: ultrafast universal RNA-seq aligner. *Bioinformatics* **29**, 15–21.
- Dow, L.E., O'Rourke, K.P., Simon, J., Tschaharganeh, D.F., van Es, J.H., Clevers, H., and Lowe, S.W. (2015). *Apc* Restoration Promotes Cellular Differentiation and Reestablishes Crypt Homeostasis in Colorectal Cancer. *Cell* **161**, 1539–1552.
- Durinck, S., Spellman, P.T., Birney, E., and Huber, W. (2009). Mapping identifiers for the integration of genomic datasets with the R/Bioconductor package *biomaRt*. *Nat. Protoc.* **4**, 1184–1191.
- Eklund, A.C., and Szallasi, Z. (2008). Correction of technical bias in clinical microarray data improves concordance with known biological information. *Genome Biol.* **9**, R26.
- Fumagalli, A., Oost, K.C., Kester, L., Morgner, J., Bornes, L., Bruens, L., Spaargaren, L., Azkanaz, M., Schelfhorst, T., Beerling, E., et al. (2020). Plasticity of *Lgr5*-Negative Cancer Cells Drives Metastasis in Colorectal Cancer. *Cell Stem Cell* **26**, 569–578.e7.
- Gautier, L., Cope, L., Bolstad, B.M., and Irizarry, R.A. (2004). *affy*-analysis of Affymetrix GeneChip data at the probe level. *Bioinformatics* **20**, 307–315.
- Gentleman, R.C., Carey, V.J., Bates, D.M., Bolstad, B., Dettling, M., Dudoit, S., Ellis, B., Gautier, L., Ge, Y., Gentry, J., et al. (2004). Bioconductor: open software development for computational biology and bioinformatics. *Genome Biol.* **5**, R80.
- Goeman, J.J., and Bühlmann, P. (2007). Analyzing gene expression data in terms of gene sets: methodological issues. *Bioinformatics* **23**, 980–987.
- Gonzalez-Roca, E., Garcia-Albéniz, X., Rodriguez-Mulero, S., Gomis, R.R., Kornacker, K., and Auer, H. (2010). Accurate expression profiling of very small cell populations. *PLoS One* **5**, e14418.
- Hothorn, T., Bretz, F., and Westfall, P. (2008). Simultaneous Inference in General Parametric Models. *Biom. J.* **50**, 346–363.
- Irizarry, R.A., Hobbs, B., Beazer-Barclay, Y.D., Antonellis, K.J., Scherf, U.W.E., and Speed, T.P. (2003). Exploration, normalization, and summaries of high density oligonucleotide array probe level data. *Biostatistics* **4**, 249–264.
- Jao, C.Y., and Salic, A. (2008). Exploring RNA transcription and turnover in vivo by using click chemistry. *Proc. Natl. Acad. Sci. USA* **105**, 15779–15784.
- Jiang, X., Hao, H.-X., Gowney, J.D., Woolfenden, S., Bottiglio, C., Ng, N., Lu, B., Hsieh, M.H., Bagdasarian, L., Meyer, R., et al. (2013). Inactivating mutations of *RNF43* confer Wnt dependency in pancreatic ductal adenocarcinoma. *Proc. Natl. Acad. Sci. USA* **110**, 12649–12654.
- Kanehisa, M., and Goto, S. (2000). KEGG: kyoto encyclopedia of genes and genomes. *Nucleic Acids Res.* **28**, 27–30.
- Kozar, S., Morrissey, E., Nicholson, A.M., van der Heijden, M., Zecchini, H.I., Kemp, R., Tavaré, S., Vermeulen, L., and Winton, D.J. (2013). Continuous clonal labeling reveals small numbers of functional stem cells in intestinal crypts and adenomas. *Cell Stem Cell* **13**, 626–633.
- Lenos, K.J., Miedema, D.M., Lodestijn, S.C., Nijman, L.E., van den Bosch, T., Romero Ros, X., Lourenço, F.C., Lecca, M.C., van der Heijden, M., van Neerven, S.M., et al. (2018). Stem cell functionality is microenvironmentally defined during tumour expansion and therapy response in colon cancer. *Nat. Cell Biol.* **20**, 1193–1202.
- Lerner, E.A., Lerner, M.R., Janeway, C.A., Jr., and Steitz, J.A. (1981). Monoclonal antibodies to nucleic acid-containing cellular constituents: probes for molecular biology and autoimmune disease. *Proc. Natl. Acad. Sci. USA* **78**, 2737–2741.
- Liao, Y., Smyth, G.K., and Shi, W. (2013). The Subread aligner: fast, accurate and scalable read mapping by seed-and-vote. *Nucleic Acids Res.* **41**, e108.
- Liao, Y., Smyth, G.K., and Shi, W. (2019). The R package Rsubread is easier, faster, cheaper and better for alignment and quantification of RNA sequencing reads. *Nucleic. Acids Res.* **47**, e47.
- Liberzon, A., Birger, C., Thorvaldsdóttir, H., Ghandi, M., Mesirov, J.P., and Tamayo, P. (2015). The Molecular Signatures Database (MSigDB) hallmark gene set collection. *Cell Syst.* **1**, 417–425.
- Liu, J., Xu, Y., Stoleru, D., and Salic, A. (2012). Imaging protein synthesis in cells and tissues with an alkyne analog of puromycin. *Proc. Natl. Acad. Sci. USA* **109**, 413–418.
- Lombardo, A., Scopelliti, A., Cammareri, P., Todaro, M., Iovino, F., Ricci-Vitiani, L., Gulotta, G., Dieli, F., de Maria, R., and Stassi, G. (2011). Bone morphogenetic protein 4 induces differentiation of colorectal cancer stem cells and increases their response to chemotherapy in mice. *Gastroenterology* **140**, 297–309.
- Love, M.I., Huber, W., and Anders, S. (2014). Moderated estimation of fold change and dispersion for RNA-seq data with DESeq2. *Genome Biol.* **15**, 550.
- Madan, B., Harmston, N., Nallan, G., Montoya, A., Faull, P., Petretto, E., and Virshup, D.M. (2018). Temporal dynamics of Wnt-dependent transcriptome reveal an oncogenic Wnt/MYC/ribosome axis. *J. Clin. Invest.* **128**, 5620–5633.
- Marco-Sola, S., Sammeth, M., Guigó, R., and Ribeca, P. (2012). The GEM mapper: fast, accurate and versatile alignment by filtration. *Nat. Methods* **9**, 1185–1188.
- Merlos-Suárez, A., Barriga, F.M., Jung, P., Iglesias, M., Céspedes, M.V., Rossell, D., Sevillano, M., Hernando-Momblona, X., da Silva-Diz, V., Muñoz, P., et al. (2011). The intestinal stem cell signature identifies colorectal cancer stem cells and predicts disease relapse. *Cell Stem Cell* **8**, 511–524.
- O'Brien, C.A., Pollett, A., Gallinger, S., and Dick, J.E. (2007). A human colon cancer cell capable of initiating tumour growth in immunodeficient mice. *Nature* **445**, 106–110.
- Pelletier, J., Thomas, G., and Volarević, S. (2018). Ribosome biogenesis in cancer: new players and therapeutic avenues. *Nat. Rev. Cancer* **18**, 51–63.
- Peltonen, K., Colis, L., Liu, H., Trivedi, R., Moubarek, M.S., Moore, H.M., Bai, B., Rudek, M.A., Bieberich, C.J., and Laiho, M. (2014). A targeting modality for

destruction of RNA polymerase I that possesses anticancer activity. *Cancer Cell* 25, 77–90.

Picelli, S., Björklund, Å.K., Faridani, O.R., Sagasser, S., Winberg, G., and Sandberg, R. (2013). Smart-seq2 for sensitive full-length transcriptome profiling in single cells. *Nat. Methods* 10, 1096–1098.

Qiu, X., Hill, A., Packer, J., Lin, D., Ma, Y., and Trapnell, C. (2017). Single-cell mRNA quantification and differential analysis with Census. *Nat. Methods* 14, 309–315.

R Development Core Team (2019). R: A language and environment for statistical computing (R Foundation for Statistical Computing).

Ricci-Vitiani, L., Lombardi, D.G., Pilozzi, E., Biffoni, M., Todaro, M., Peschle, C., and De Maria, R. (2007). Identification and expansion of human colon-cancer-initiating cells. *Nature* 445, 111–115.

Ritchie, M.E., Phipson, B., Wu, D., Hu, Y., Law, C.W., Shi, W., and Smyth, G.K. (2015). limma powers differential expression analyses for RNA-sequencing and microarray studies. *Nucleic Acids Res.* 43, e47.

Robichaud, N., and Sonenberg, N. (2017). Translational control and the cancer cell response to stress. *Curr. Opin. Cell Biol.* 45, 102–109.

Robichaud, N., Sonenberg, N., Ruggero, D., and Schneider, R.J. (2019). Translational Control in Cancer. *Cold Spring Harb. Perspect. Biol.* 11, a032896.

Ruggero, D. (2012). Revisiting the nucleolus: from marker to dynamic integrator of cancer signaling. *Sci. Signal.* 5, pe38.

Sanz-Pamplona, R., Berenguer, A., Cordero, D., Molleví, D.G., Crous-Bou, M., Sole, X., Paré-Brunet, L., Guino, E., Salazar, R., Santos, C., et al. (2014). Aberrant gene expression in mucosa adjacent to tumor reveals a molecular crosstalk in colon cancer. *Mol. Cancer* 13, 46.

Satija, R., Farrell, J.A., Gennert, D., Schier, A.F., and Regev, A. (2015). Spatial reconstruction of single-cell gene expression data. *Nat. Biotechnol.* 33, 495–502.

Schindelin, J., Arganda-Carrera, I., Frise, E., Verena, K., Mark, L., Tobias, P., Stephan, P., Curtis, R., Stephan, S., Benjamin, S., et al. (2009). Fiji: an open-source platform for biological-image analysis. *Nat. Methods* 9, 676–682.

Shimokawa, M., Ohta, Y., Nishikori, S., Matano, M., Takano, A., Fujii, M., Date, S., Sugimoto, S., Kanai, T., and Sato, T. (2017). Visualization and targeting of LGR5⁺ human colon cancer stem cells. *Nature* 545, 187–192.

Signer, R.A.J., Magee, J.A., Salic, A., and Morrison, S.J. (2014). Haematopoietic stem cells require a highly regulated protein synthesis rate. *Nature* 509, 49–54.

Smyth, G.K. (2004). Linear models and empirical bayes methods for assessing differential expression in microarray experiments. *Stat. Appl. Genet. Mol. Biol.* 3, 3.

Subramanian, A., Tamayo, P., Mootha, V.K., Mukherjee, S., Ebert, B.L., Gillette, M.A., Paulovich, A., Pomeroy, S.L., Golub, T.R., Lander, E.S., and Mesirov, J.P. (2005). Gene set enrichment analysis: a knowledge-based approach for interpreting genome-wide expression profiles. *Proc. Natl. Acad. Sci. USA* 102, 15545–15550.

Tauriello, F., Palomo-Ponce, S., Stork, D., Berenguer-Llergo, A., Badia-Ramentol, J., Iglesias, M., Sevillano, M., Ibiza, S., Cañellas, A., Hernando-Mombona, X., et al. (2018). TGF β drives immune evasion in genetically reconstituted colon cancer metastasis. *Nature* 554, 538–543.

van de Wetering, M., Sancho, E., Verweij, C., de Lau, W., Oving, I., Hurlstone, A., van der Horn, K., Batlle, E., Coudreuse, D., Haramis, A.P., et al. (2002). The beta-catenin/TCF-4 complex imposes a crypt progenitor phenotype on colorectal cancer cells. *Cell* 111, 241–250.

van de Wetering, M., Francies, H.E., Francis, J.M., Bounova, G., Iorio, F., Pronk, A., van Houdt, W., van Gorp, J., Taylor-Weiner, A., Kester, L., et al. (2015). Prospective derivation of a living organoid biobank of colorectal cancer patients. *Cell* 161, 933–945.

van der Heijden, M., Miedema, D.M., Waclaw, B., Veenstra, V.L., Lecca, M.C., Nijman, L.E., van Dijk, E., van Neerven, S.M., Lodestijn, S.C., Lenos, K.J., et al. (2019). Spatiotemporal regulation of clonogenicity in colorectal cancer xenografts. *Proc. Natl. Acad. Sci. USA* 116, 6140–6145.

Vermeulen, L., Todaro, M., de Sousa Mello, F., Sprick, M.R., Kemper, K., Perez Alea, M., Richel, D.J., Stassi, G., and Medema, J.P. (2008). Single-cell cloning of colon cancer stem cells reveals a multi-lineage differentiation capacity. *Proc. Natl. Acad. Sci. USA* 105, 13427–13432.

Vermeulen, L., De Sousa E Melo, F., van der Heijden, M., Cameron, K., de Jong, J.H., Borovski, T., Tuynman, J.B., Todaro, M., Merz, C., Rodemond, H., et al. (2010). Wnt activity defines colon cancer stem cells and is regulated by the microenvironment. *Nat. Cell Biol.* 12, 468–476.

Witte, D.P., Wiginton, D.A., Hutton, J.J., and Aronow, B.J. (1991). Coordinate developmental regulation of purine catabolic enzyme expression in gastrointestinal and postimplantation reproductive tracts. *J. Cell Biol.* 115, 179–190.

Wu, D., Lim, E., Vaillant, F., Asselin-Labat, M.-L., Visvader, J.E., and Smyth, G.K. (2010). ROAST: rotation gene set tests for complex microarray experiments. *Bioinformatics* 26, 2176–2182.

STAR★METHODS

KEY RESOURCES TABLE

REAGENT or RESOURCE	SOURCE	IDENTIFIER
Antibodies		
Goat Anti Mouse EphB2	R&D systems	Cat# AF467; RRID: AB_355375
Goat Anti Human EpCAM /TROP-1	R&D systems	Cat# AF960; RRID: AB_355745
Anti-Ki67	BD Biosciences	Cat# 550609; RRID: AB_393778
RPA194 (C-1) antibody	Santa Cruz	Cat# sc-48385; RRID: AB_675814
tdTomato polyclonal antibody	Sicgen	Cat# AB8181-200; RRID: AB_2722750
Anti-RFP/tdTomato antibody	Rockland	Cat# 600-401-379; RRID: AB_2209751
GFP antibody	Abcam	Cat# ab183734; RRID: AB_2732027
Cytokeratin 20 antibody	Dako	Cat# M7019; RRID: AB_2133718
Anti-Mouse CD16 / CD32	Tonbo Biosciences	Cat# 70-0161; RRID: AB_2621487
BV421 Rat Anti-Mouse CD31 Clone MEC 13.3	BD Biosciences	Cat# 562939; RRID: AB_2665476
BV421 Mouse CD45RB Clone 16A	BD Biosciences	Cat# 562849; RRID: AB_2737836
CD326 (EpCAM) Monoclonal Antibody (1B7), PE-Cyanine7	Thermo Fisher Scientific	Cat# 25-9326-42; RRID: AB_2573542
CD326 (EpCAM)-APC-Vio770 human antibody	Miltenyl Biotec	Cat# 130-101-161; RRID: AB_2660308
APC/Cyanine7 anti-mouse CD326 (EpCAM) antibody	Biologends	Cat# 118217; RRID: AB_1501158
APC anti-human EphB2 antibody (2H9 clone)	BD Biosciences	Cat# 564699; RRID: AB_2738898
rRNA(5.8S)(Y10b)	Thermo Fisher Scientific	Cat# MA1-13017; RRID: AB_10979967
Donkey anti-Goat conjugated to Alexa 488/568/647	Thermo Fisher Scientific	Cat# A11055; RRID: AB_2534102 Cat# A11057; RRID: AB_142581 Cat# A21447; RRID: AB_141844
Donkey anti-Rabbit conjugated to Alexa 488/568/647	Thermo Fisher Scientific	Cat# A21206; RRID: AB_2535792 Cat# A10042; RRID: AB_2534017 Cat# A31573; RRID: AB_2536183
Donkey anti-Mouse conjugated to Alexa 488/568/647	Thermo Fisher Scientific	Cat# A21202; RRID: AB_141607 Cat# A10037; RRID: AB_2534013 Cat# A31571; RRID: AB_162542
BightVision poly-HRP anti-Rabbit	Immunologic	DPVR-110HRP

(Continued on next page)

Continued

REAGENT or RESOURCE	SOURCE	IDENTIFIER
Rabbit anti-RRN3	Sigma-Aldrich/Merck	HPA049837
Mouse anti-bActin	Abcam	20272
KRT20	Atlas Antibodies	HPA024309
Goat anti-Rabbit Alexa Fluor 680	Thermo Fisher Scientific	A-21076
Biological Samples		
Patient derived organoids (PDOs)	(van de Wetering et al., 2015) Giorgio Stassi Laboratory (Lombardo et al., 2011)	N/A
Mouse derived organoids (shAPC-KP)	(Dow et al., 2015)	N/A
Experimental Models: Cell Lines		
LS174T	ATCC	CL-188
SW403	ATCC	CCL-230
Chemicals, Peptides, and Recombinant Proteins		
Tamoxifen	Sigma-Aldrich/Merck	T5648
4-hydroxytamoxifen	Peptotech Sigma-Aldrich/Merck	6833585 H7904
Doxycycline hyclate	Sigma-Aldrich/Merck	D9891
5-Fluorouracil (5-FU)	Sigma-Aldrich/Merck	F6627
Irinotecan	Sigma-Aldrich/Merck	I1406
Leucovorin	Sigma-Aldrich/Merck	47612
TrypLE Express Enzyme (1X)	Thermo Fisher Scientific	12604039
Trypsine	Thermo Fisher Scientific	25300054
DMEM high glucose pyruvate	Thermo Fisher Scientific	41966052
Advanced-DMEM/F-12	Thermo Fisher Scientific	12634028
Matrigel growth factor reduced	Corning	356231
Cultrex Growth Factor Reduced BME2	Amsbio	3533-010-02
HEPES	Thermo Fisher Scientific	15630056
Glutamax	Thermo Fisher Scientific	35050-038
B-27 Supplement	Thermo Fisher Scientific	12587-010
N-Acetyl-L-cysteine	Sigma-Aldrich/Merck	A7250-
Nicotinamide	Sigma-Aldrich/Merck	72340
EGF	Peptotech	AF-100-15
bFGF	Thermo Fisher Scientific	PHG0026
Noggin	In house	N/A
R-spondin	In house	N/A
Rock inhibitor, Y-27632	Med Chem express	HY-10583
Gastrin I	Tocris	3006
TGFb-RI inhibitor, A83-01	Tocris	2939
P38a/b inhibitor, SB202190 monohydrochloride hydrate	Sigma-Aldrich/Merck	S7076
TGFb-RI inhibitor (galunisertib), LY2157299	In house	N/A
Chemical Inducer of Dimerization, AP20187	Med Chem express	HY-13992
5-Ethynyl-2'-deoxyuridine (EdU)	Thermo Fisher Scientific	A10044
5-Ethynyl uridine (EU)	Click chemistry Tools	1261-100
O-propargyl-puromycin (OPP)	Medchem Source	JA-1024
L-homopropargylglycine (HPG)	Click chemistry Tools	1067-100
Polymerase I inhibitor, BMH-21	Invivochem	V1435
Cell recovery solution	Corning	354253

(Continued on next page)

Continued

REAGENT or RESOURCE	SOURCE	IDENTIFIER
Proteinase K	Thermo Fisher Scientific	25530049
IRDye 800CW Azide Infrared Dye	Li-COR (Bonsai Advanced Technologies)	929-60000
Smart-seq2 lysis buffer	In house Picelli et al., 2013	N/A
Critical Commercial Assays		
High-Capacity cDNA Reverse Transcription kit	Thermo Fisher Scientific	4368813
Nucleospin Plasmid QuickPure Miniprep Kit	Cultek	740615250
PureLink® RNA Mini Kit	Thermo Fisher Scientific	12183025
GenElute Mammalian Genomic DNA Miniprep Kit	Sigma-Aldrich/Merck	G1N70-1KT
Cell Line Nucleofector® Kit V	Cultek (Lonza)	VCA-1003
Click-iT Edu Alexa Fluor 647 Imaging Kit	Thermo Fisher Scientific	C10340
Click-iT RNA Alexa Fluor 488 Imaging Kit	Thermo Fisher Scientific	C10329
Click-iT Plus OPP Alexa Fluor 594 Protein Synthesis Assay Kit	Thermo Fisher Scientific	C10457
SuperSignal West Pico Chemiluminescent Substrate	Thermo Fisher Scientific	34080
GeneChip Human PrimeView array	Affymetrix	901837
GeneChip Mapping 250 K Nsp assay kit	Affymetrix	900753
GeneChip Hybridization Wash and Stain Kit	Affymetrix	900720
GeneChipFluidics Station 450	Affymetrix	00-0377
High sensitivity DNA Kit	Agilent Technologies	5067-4626
Nextera® XT DNA Library Prep Kit ® XT	Illumina	FC-131-1024
MegaPrime labeling kit	GE Healthcare	RPN1604
Reagent or Resource		
SYBR® Green PCR Master Mix	Thermo Fisher Scientific	4368706
TaqMan® Universal PCR Master Mix	Thermo Fisher Scientific	4364341
Phusion High Fidelity DNA Polymerase	Thermo Fisher Scientific	F530L
DNA Polymerase	Biotools	10.014
SuperScript II Reverse Transcriptase	Thermo Fisher Scientific	18064022
Agencourt Ampure XP beads	Beckman coulter	A63880
KAPA HiFi Hotstart ReadyMix	Roche	KR0370
Trizol	Thermo Fisher Scientific	15596018
Schiff's Reagent	Panreac	171588.1609
Alcian Blue solution	Panreac	CA254584.1604
DPX	Panreac	255254
Peroxidase blocking solution	Dako	S202386
Envision Flex antibody diluent	Agilent	K8006
Normal Donkey Serum	Jackson Immunoresearch	017-000-121
Normal Goat Serum	Jackson immunoresearch	005-000-121
DAPI-Fluoromount-G Mounting Medium	Southern Biotech	0100-20
NucBlue Live ReadyProbes Reagent, Hoechst	Thermo Fisher Scientific	R37605

(Continued on next page)

Continued

REAGENT or RESOURCE	SOURCE	IDENTIFIER
Oligonucleotides		
sgRNA guides	This paper	Table S1
Genotyping	This paper	Table S2
Southern probes	This paper	Table S3
Taqman primers	This paper	STAR Methods
Deposited Data		
Microarrays and RNA-seq	This paper	GEO: GSE125232
Single cell RNA-seq	This paper	GEO: GSE148345
Software and Algorithms		
FlowJo	BD Biosciences	https://flowjo.com
NDP.view2	N/A	https://www.hamamatsu.com
Fiji	Schindelin et al., 2009	https://imagej.net/Fiji
GraphPad Prism	Prism software	RRID: SCR_002798
Illustrator CS6	Adobe	RRID: SCR_010279
StepOne 2.2 plus and SDS2.4	Thermofisher	https://www.thermofisher.com/es/es/home.html
BD FACS Diva Software	BD Biosciences	RRID: SCR_001456
ScanR Software	N/A	www.olimpus-lifesciences.com/en/microscopes/inverted/scanr/
Zeiss LSM 780 Software	N/A	https://www.zeiss.com
QuPath	N/A	https://qupath.github.io/
R language and environment for statistical computing	R Development Core Team (2019)	https://cran.r-project.org/
affy package	Gautier et al., 2004	https://bioconductor.org
affy PLM package	Bolstad et al., 2005	https://bioconductor.org
Limma R package	Ritchie et al., 2015	https://bioconductor.org
STAR version 2.7.0a	Dobin et al., 2013	https://github.com
R package Rsubread	Liao et al., 2019	https://bioconductor.org
R package BiomaRt	Durinck et al., 2009	https://bioconductor.org
DESeq2 R package	Love et al., 2014	https://bioconductor.org
GSEA	Subramanian et al., 2005	https://www.gsea-msigdb.org/gsea/index.jsp
FastQC Suite	N/A	https://www.bioinformatics.babraham.ac.uk
GEMT Tools 1.7.0.	Marco-Sola et al., 2012	http://gemtools.github.io
Seurat package 2.3.4	Satija et al., 2015	https://bioconductor.org
Monocle package 2.8.0	Qiu et al., 2017	https://bioconductor.org
lme4 R package	Bates et al., 2014	https://cran.r-project.org
Multcomp R package	Hothorn et al., 2008	https://cran.r-project.org

RESOURCE AVAILABILITY

Lead Contact

Further information and requests for resources and reagents should be directed to and will be fulfilled by the Lead Contact, Eduard Batlle (eduard.batlle@irbbarcelona.org).

Materials Availability

Knock-in CRC organoids and NTCF4 expressing CRC cell lines generated in this study are available from the Lead Contact with a completed Materials Transfer Agreement.

Data and Code Availability

Expression arrays and RNA-seq data are available at Gene Expression Omnibus (GEO). The accession number for the expression arrays reported in this paper is GEO: GSE125232 and for the scRNA-seq data it is GEO: GSE148345. Computer code is available upon request.

EXPERIMENTAL MODEL AND SUBJECT DETAILS

Mouse strains and tumor cell injections

All experiments with mouse models were approved by the Animal Care and Use Committee of Barcelona Science Park (CEEA-PCB) and the Catalan government. To generate subcutaneous xenografts from PDOs we inoculated 150,000 (PDO7), 50,000 (PDO p19b) or 1.5 million cells (PDO-p18) in a format of 4-5 days grown undissociated organoids into Beige (CB17.*Cg-PrkdcscidLystbg-J/Crl*) or NSG (NOD.*Cg-Prkdc < scid > Il2rg < tm1Wjl > /SzJ*) female mice in 100 μ l of 50% BME2-HBSS (Cultrex). For mouse-derived AKP xenografts, 5000 cells in 100 μ l of 50% matrigel-HBSS (Corning) were injected into the flanks of Swiss nude (*Crl:NU(lco)-Fox1nu*) female mice. Cell number was determined by trypsinizing and counting an aliquot of a total cellular suspension. Tumor volume was measured with manual calipers and calculated according to the formula (length x width x height)/2. To generate liver metastasis, dissociated organoids (single cells) were injected intrasplenically (IS) in NSG mice as described in [Calon et al. \(2012\)](#) and [Tauriello et al. \(2018\)](#). Cells were counted and resuspended in HBSS for injection using 0.5×10^6 cells in 70 μ l per mouse. For tumor initiation assays, viable single cells from disaggregated xenografts were sorted according to their EGFP-POLR1A levels and transplanted subcutaneously into Beige/NSG recipient mice in 100 μ l of 50% BME2-HBSS. For metastasis initiation experiments, viable single cells from disaggregated xenografts were FACS sorted according to their POLR1A-tdTomato levels and transplanted intrasplenically in NSG mice in 70 μ l of HBSS.

In vivo treatments

For inducible ablation experiments, we treated animals with 5mg/kg of dimerizer (AP20187, Medchem express, HY-13992) when tumors reached an average size of 40-50 mm³. For acute treatments (5-10 days) animals were treated daily and for chronic treatments (> 10 days) every 2-3 days. Control animals were treated with vehicle for the same period of time. For *in vivo* reversibility experiments, mice bearing subcutaneous AKP xenografts were given 2 mg/ml DOX in drinking water until tumors reached a size of about 50mm³. After that, DOX was removed for the indicated periods (8 days ON or 20 days APC-ON) before mice were given DOX again (APC-OFF). To induce Cre-mediated recombination of the tdTomato cassette for lineage tracing experiments, mice bearing subcutaneous tumor xenografts (50-70mm³) received a single intraperitoneal tamoxifen (Sigma) injection of 1mg/kg for KRT20 and 10mg/kg for POLR1A or two consecutive intraperitoneal tamoxifen injections of 250mg/kg for LGR5. For experiments with small molecule RNA polymerase I inhibitor, BMH21 (Invivochem), we injected intraperitoneally a daily dose of 100 mg/Kg over the period of 10 days once tumors had reached an average size of 50 mm³. Control animals were treated with vehicle over the same period. For chemotherapy experiments subcutaneous tumor xenografts were generated by inoculating POLI-iCT PDO7 or PDO-p18 knock-in organoids. Once tumors reached an average size of 70mm³ animals were treated with three intraperitoneal injections of folfiri (100 μ l/20 gr) at day 0, 3 and 7. Folfiri cocktail contained 5-FU (30mg/kg), Irinotecan (24mg/kg) and Leucovorin (90mg/kg). Control animals were treated with vehicle following the same regimen. Animals were sacrificed the last day of treatment and tumors were removed and processed for FACS and histological analysis. In all experiments animals were sacrificed at indicated time points or just before tumor size reached the volume permitted by Animal Facility regulations. In all animal treatments, individuals were randomized.

Orthotopic models and primary CRC samples

Patient-derived orthotopic xenografts (PDOX1 and PDOX2) were generated from fresh biopsies taken from peritoneal implants at tumor relapse after FOLFOX chemotherapy treatment from Hospital Universitari de Bellvitge (L'Hospitalet de Llobregat) and Hospital Moisès Broggi (Sant Joan Despí) from Barcelona. Orthotopic implantation procedure of colorectal human tumors was performed as described previously ([Aytes et al., 2012](#)). At the time of sacrifice mice implanted with PDOX2 tumor presented a synchronic hepatic metastasis that was isolated and implanted orthotopically into the liver of other four animals (PDOX2-MH). All patients gave written consent to participate in the study, and The Ethics Committee of the hospitals approved the study protocol. Animals were kept under pathogen-free conditions, and all animal work was conducted according to the guidelines from the Animal Care Committee at the Generalitat de Catalunya (Procedure 9111) in the Animal Core Facility of IDIBELL (AAALAC Unit 1155). The study was approved by the IDIBELL Ethical Committee and performed in accordance with guidelines stated in The International Guiding Principles for Biomedical Research involving Animals, developed by the Council for International Organizations of Medical Sciences (CIOMS). For the purification of EPHB2 tumor cell populations, fresh surgically resected Human CRC samples (n = 10) were obtained from individuals treated at Hospital Clínic (Barcelona). Tumors were disaggregated following the protocol detailed in ([Calon et al., 2012](#)) and EPHB2 populations were purified as described in ([Merlos-Suárez et al., 2011](#)). For the 5.8S and KRT20 analysis, formalin-fixed, paraffin-embedded tissue sections of primary human colorectal adenocarcinomas (n = 24) were obtained from the biobank of the Servei de Patologia from Hospital del Mar (MARBiobanc, Barcelona). Samples were obtained under informed consent and approval of the Tumor Bank Committees according to Spanish ethical regulations. The study followed the guidelines of the Declaration of Helsinki, and patient identity for pathological specimens remained anonymous in the context of this study.

Organoid *in vitro* culture

Patient-derived organoids (PDOs) were cultured as described in Cortina et al. (2017) and van de Wetering et al. (2015). PDO7 was obtained from Prof. Stassi laboratory (Lombardo et al., 2011), PDO-p18 and PDO-p19b from Prof. Clevers laboratory (van de Wetering et al., 2015) and AKP (shAPC-KP) organoids were a kind gift from Dr. Luke Dow's laboratory. AKP organoids were embedded in Matrigel (Corning) and grown in Advanced DMEM/F12 supplemented with 10 mM HEPES, 2 mM GlutaMAX, B27, recombinant Noggin (100 ng/ml), EGF (50 ng/ml, Preprotech), and in the presence of Doxycycline (DOX, 2 μ g/mL), (APC OFF) or absence (APC ON) to induce differentiation (Dow et al., 2015) at indicated time points. PDOs were embedded in a mixture of 70% BME2 and 30% Advanced DMEM/F12 with HEPES and GlutaMAX. PDO-p18 and PDO-p19b were cultured as described by the Clevers laboratory (van de Wetering et al., 2015) and PDO7 as described in Cortina et al. (2017).

N-TCF4 expressing CRC cells lines

LS174T and SW403 CRC cell lines obtained from ATCC were engineered to express a tamoxifen-inducible dominant negative form of TCF4 which consists in the β -catenin-binding domain of TCF4 fused to a modified hormone-binding domain of the estrogen receptor (nTCF-ERT2)(van de Wetering et al., 2002). CRC cell lines expressing the nTCF-ERT2 construct were cultured under standard conditions (DMEM with 10% FBS) (Wnt ON) and when indicated, were treated with 1 μ M 4-hydroxytamoxifen (Merck H7904) (Wnt OFF). In all experiments, we only used the modified cell lines, and for simplicity we refer to them as LS174T and SW403 respectively, although both express nTCF-ERT2 construct.

METHOD DETAILS

Organoid formation experiments

To run organoid formation experiments we used single cells obtained either by trypsinization from an *in vitro* experiment, or by FACS sorting from subcutaneous tumor xenografts. For the AKP organoid formation experiments, AKP organoids embedded in Matrigel were grown in the presence of DOX (APC OFF) or without DOX (APC ON) for the indicated periods (2 days ON, 5 days ON). Then, organoids were disaggregated to a single cell suspension using TrypLE reagent (GIBCO), and seeded in 25 μ L Matrigel drops containing 1000 cells/drop, and DOX was added to the medium in all conditions indicated with /OFF. To assess POLR1A organoid formation capacity, we disaggregated xenografts as described below and living cells were selected for EPCAM expression and sorted according to their endogenous POLR1A levels by FACS. Afterward, single cells were seeded *in vitro* in 25 μ L BME2 drops containing 1000 cells/drop per condition. To test the effect of BMH21 *in vitro*, single cells obtained by trypsinization from *in vitro* culture were seeded in 25 μ L BME2 drops containing 1000 cells/drop per condition and were treated daily with BMH-21 (1 μ M). Control plates were treated with vehicle and growth was measured using the method described below. In all cases, plates were scanned using ScanR inverted microscope (Olympus) at day 1 post-seeding to quantify the exact number of cells seeded per drop and at the experimental endpoint (day 7 post-seeding). Full drops were scanned taking overlapping pictures at 4x magnification and at 8 different z stacks with a separation of 200 μ m. Z stacks of all images were projected into a single image and the full drop was digitally reconstructed by stitching the different image projections using an ImageJ (Schindelin et al., 2009) custom-made macro developed for this purpose. Total number and mean size of cells (i.e., any object with a diameter larger than 5 μ m) or organoids (diameter larger than 400 μ m) were counted. Differences were assessed with Student's t test.

Immunostaining and confocal imaging

CRC cell lines grown on ethanol-sterilized glass coverslips were washed three times with PBS and incubated with 4% paraformaldehyde (PFA) for 15 min at room temperature, washed again with PBS and incubated for additional 5 min with 50 mM NH_4Cl to quench PFA's auto-fluorescence. Blocking and permeabilization were performed simultaneously for 1 h at room temperature in PBS containing 3% BSA and 0.3% Triton X-100. Coverslips were first incubated in a humid chamber overnight at 4°C with primary antibody diluted in the blocking/permeabilization solution. After extensive washing, the incubation with the secondary antibody was done for 1 h in the dark. In the case of co-staining, both primary and secondary antibodies were mixed and used at the same time. Coverslips were mounted with DAPI-Fluoromount-G (SouthernBiotech, 0100-20). For live imaging, PDOs were seeded in 10 μ L drops of BME2 in 8-well chamber coverslip (IBIDI) and covered with 200 μ L of the corresponding culture medium. 4-5 days grown organoids were directly incubated 30 min at 37°C with Hoechst 33342 1:1000 (Molecular Probes, R37605) prior to confocal visualization. For immunostainings, PDOs were seeded in microscopy chamber slides in thin layers of BME2 (20 μ L per chamber). Samples were then fixed with 4% PFA for 15 min and quenched with 20 mM glycine for 20 min. Permeabilization was achieved with 0.5% Triton X-100 for 30 min at room temperature, then a second blocking step with 1% BSA for 1 h at room temperature was performed. Samples were incubated with primary antibodies overnight at 4°C in a dark chamber followed by incubation with the correspondent secondary antibody for 1 h at room temperature in the dark. Washes were performed between each step with PBS. Coverslips were mounted with DAPI-Fluoromount-G. To visualize OP-P (Medchem Source LLP, JA-1024), EU (Click Chemistry Tools, 1261-100), and HPG (Click Chemistry Tools, 1067-100), slides were incubated with Click-it cocktail kit (Thermo Fisher) for 30 min in dark prior to antibody staining. Primary and secondary antibodies used for *in vitro* immunostaining were the same as the ones described for IF in paraffin sections. For paraffin-included organoid pellets, Matrigel drops were washed twice with PBS, incubated with formalin for 2h at RT, washed again with PBS, and left overnight in formalin at 4°C. The next day, two more washes with PBS were performed, and drops were put into a microcassette (Leica). Microcassettes were put into a regular histological cassette before paraffin embedding.

Immunostainings were performed as described in histology and tissue staining section. Images were taken with a Zeiss LSM780 confocal microscope. Whole organoid z stacks were taken with a LEICA SP5 microscope. Next, images were background-subtracted and maximum intensity projections were rendered by Imaris software version 9.1.

Histology and tissue stainings

Immunostainings were performed on 4 μm sections following a standard protocol. For PAS/Alcian Blue staining, samples were deparaffinated and rehydrated, followed by 5 min incubation with Alcian Blue solution pH 2.5 (1 g of Alcian Blue (Panreac), 97 mL milliQ water, 100 mL glacial acetic acid) and dehydrated with ethanol 96%. Samples were rehydrated again, washed with distilled water, incubated with 1% periodic acid for 20 min, washed with tap water, incubated for 20 min with Schiff's reagent (Sigma), washed with distilled water, and counterstained with hematoxylin prior to dehydrating and mounting with DPX (Panreac, 255254.1608). For immunohistochemistry (IHC), antigen retrieval was carried out by boiling in Tris-EDTA buffer for 20 min, then samples were blocked with Peroxidase-Blocking Solution (Dako: S202386) followed by blocking with normal goat serum 10% (Jackson ImmunoResearch, 005-000-121) in wash buffer 1X and incubated with primary antibody against TdTomato (rabbit, Rockland, 600-401-379) 1:200 in Envision FLEX antibody diluent (Agilent, K8006) at 4°C overnight. Secondary antibody BrightVision poly-HRP anti-Rabbit (Immunologic, DPVR-110HRP) was added for 30 min at room temperature. Slides were counterstained with hematoxylin prior to dehydrating and mounting with DPX (Panreac, 255254.1608). Washes were performed between steps with wash buffer 1X (Dako, K800721). To visualize OP-P, EU, and HPG, slides were incubated with Click-it cocktail kit (Thermo Fisher, 100 μl per slide) for 30 min in dark prior antibody staining. For immunofluorescence the applied protocol was the same as for IHC but blocking with normal donkey serum 10% (Jackson ImmunoResearch, 017-000-121) in wash buffer 1X with the following primary antibodies diluted in Envision FLEX antibody diluent (Agilent, K8006): 1:50 EPHB2 (goat, R&D systems, AF467), 1:50 EPCAM-Trop1 (goat, R&D, AF960), 1:100 KI67 (mouse, BD, 550609), 1:50 5.8S (mouse, Thermo Fisher, MA1-13017), 1:100 POLR1A (mouse, Santa Cruz, sc-48385), 1:200 tdTomato or RFP (goat, Sicgen, AB8181-200), 1:200 EGFP (rabbit, abcam, ab183734), 1:50 KRT20 (mouse, Dako, M7019), and secondary antibodies: donkey anti-goat conjugated to Alexa 488/568/647 (Life Technologies A11055, A11057, A21447), donkey anti-rabbit conjugated to Alexa 488/568/647 (Life Technologies A21206, A10042, A31573) and donkey anti-mouse conjugated to Alexa 488/568/647 (Life Technologies A-21202, A10037, A31571) at 1:400 for 1h at RT. DAPI was added at 1:2500 after secondary antibody incubation and slides were mounted with Fluorescent mounting medium (Dako, 53023). For *in situ* hybridization paraffin sections of human tissues were de-waxed and hydrated following standard procedures. Samples were then treated with 0.2N HCl for 15min at room temperature, washed 3X in PBS and incubated for 20min at 37°C in Proteinase K (30 $\mu\text{g}/\text{ml}$ in PBS). 0.2% glycine in PBS was added for 3 minutes to neutralize Proteinase K activity and samples were then washed 2X in PBS. Sections were postfixed in 4% PFA for 10 min and washed 3X in PBS. Histone acetylation was performed by incubating the samples 2X 5 min in an H_2O solution containing 1.5% triethanolamine, 0.15% HCl and 0.6% Acetic anhydride. Samples were then washed and prehybridized for 1h at 70°C in prehybridization solution (50% Formamide, 5X SSC, 2% Blocking Reagent (Roche), 0.05% CHAPS, 5mM EDTA, 50 $\mu\text{g}/\text{ml}$ Heparin and 50 $\mu\text{g}/\text{ml}$ yeast RNA). For Lgr5 ISH, mRNA probe was diluted 500ng/ml in prehybridization solution and incubated for 48h at 65°C. Post-hybridization washes were performed 3X 20 min in 50% Formamide / 2XSSC at 65°C. Sections were then rinsed in TBST buffer (0.1M Tris-HCl pH7.5, 0.15M NaCl, 0.1% Tween20) and blocked for 30 min at room temperature in Blocking buffer (0.5% Blocking Reagent, 10% sheep serum in TBST). Sheep anti-DIG antibody (Roche) was diluted 1/5000 in blocking buffer and incubated overnight at 4°C. Finally, samples were washed in TBST and then in NTM buffer (0.1M Tris pH9.5, 0.1M NaCl, 0.05 M MgCl_2) and developed in NBT/BCIP solution (Roche) for 24-72h.

Histological Image Acquisition

Digital scanned brightfield and fluorescent images were acquired with a NanoZoomer-2.0 HT C9600 scanner (Hamamatsu, Photonics, France) equipped with a 20X objective and using NDP.scan2.5 software U10074-03 (Hamamatsu, Photonics, France). Fluorescent images were acquired with a mercury lamp unit L11600-05 couple to the NanoZoomer. All images were visualized with the NDP.view 2 U123888-01 software (Hamamatsu, Photonics, France) with a gamma correction set at 1.8 in the image control panel. In each batch of samples, the same exposure time and gain per antibody have been used. All images were visualized with a gamma correction set at 1.0 and the sharpen filter enabled in the image controls panel of the NDP.view 2 U12388-01 software.

sgRNA design

Small guide RNAs were designed < 15bp around the intended site of knock-in insertion using the <http://crispr.mit.edu> web tool and were cloned into a pX330-IRFP hSpCas9 plasmid (Cortina et al., 2017) as described in <http://www.genome-engineering.org/crispr/wp-content/uploads/2014/05/CRISPR-Reagent-Description-Rev20140509.pdf>. The sgRNA sequences are available in Table S1.

Donor plasmid construction

750bp (LGR5, KRT20, POLR1A and AAVS1 constructs) of 5' and 3' homology arm (HA) flanking the knock-in insertion cassettes were amplified from PDO7 gDNA or synthesized by gene synthesis (Thermo Fisher) and cloned into pShuttle or pDONOR vectors. Homology arms EGFP-linker, LF2A-CreERT2-BGHpA, Lox-tagBFP-3xpA-Lox-tdTomato-BGHpA insertion cassettes were generated by gene synthesis (Thermo Fisher) and cloned in the 5'HA-3'HA previously engineered pShuttle or pDONOR vectors (as described in Cortina et al., 2017).

For the *LGR5-iCaspase9-T2A-tdTomato* donor (pDONOR-LGR5-iCT), a previously described p-shuttle-LGR5-LF2A-CreERT2 plasmid (Cortina et al., 2017) was modified by replacing the existing LGR5 5' homology arm with a LGR5 5' homology arm containing a STOP codon using *PacI* and *Sall*. Subsequently, the plasmid was digested with *SgrDI* and *NotI*-HF to substitute the LF2A-CreERT2 cassette with an IRES-iCasp9-T2A-TdTom-WPRE cassette, amplified by PCR from a plasmid obtained from T.Sato's laboratory (Shimokawa et al., 2017). For the *LGR5-iCaspase9-T2A-EGFP* version, TdTomato was then replaced by EGFP by digesting with *KflI* and *MluI*, and introducing in-frame an iCasp9 fragment-T2A-EGFP, amplified by PCR from a custom gene synthesis DNA string (Thermo Fisher).

For *POLR1A-iCaspase9-T2A-tdTomato*, the human *POLR1A* 5' homology arm was cloned in the place of the LGR5 5' homology arm in pDONOR-LGR5-iCT donor vector by *PacI* and *SgrDI* digestion. The 3' homology arm was cloned by *NotI*-HF and *AscI* digestion. Inserts were amplified by PCR from custom gene synthesis DNA strings (Thermo Fisher).

Generation of CRISPR-Cas9 knock-in PDOs

PDOs were cultured and CRISPR-Cas9 knock-in editing was carried out as described in Cortina et al. (2017). In brief, to obtain PDOs expressing endogenous EGFP-POLR1A fusion protein we designed a sgRNA targeting a sequence flanking the TSS (or transcription start site) of the *POLR1A* locus. For the lineage tracing and the inducible caspase9 knock-in generation, sgRNA sequences were designed to bind the 3'UTR. After nucleofection with guide-Cas9 and donor plasmids (Cortina et al., 2017), single cell clones were derived and PCR screened for correct integration. Southern blotting was performed to assess off-target integrations. For each knock-in construct, we evaluated that the fluorescent cassette reported the expression of the gene of interest by RT-qPCR *in vitro* and *in vivo* in a similar manner as performed in Cortina et al. (2017).

Genotyping PCR and Southern blot

Single-cell derived clones were lysed in 10 mM Tris, 1 mM EDTA, 1% Tween 20 and 0.4 mg/mL proteinase K lysis buffer for 1h at 55°C, and the enzyme was inactivated for 10' at 95°C. 2 μ L of the lysate were directly used in the specific integration PCR. For the 5' specific integration PCR, a forward primer binding gDNA upstream of the 5' homology arm and a reverse primer at the beginning of the inserted cassette were used. Similarly, for the 3' specific integration PCR a forward primer at the end of the inserted cassette and a reverse primer downstream of the 3' homology arm were used. Primer sequences used are shown in Table S2. For Southern blot, genomic DNA was extracted using the GenElute Mammalian Genomic DNA Miniprep Kit (Sigma G1N70-1KT). 10 μ g of genomic DNA were digested overnight with the appropriate restriction enzyme (Table S3) and separated on a 0.8% agarose gel. DNA fragments were transferred by capillarity to a Hybond-N+ membrane (GE Healthcare RPN303B) overnight. Probes were generated by PCR and radioactively labeled with α -[32P] dCTP using the MegaPrime labeling kit (GE Healthcare RPN1604). Hybridization with the probe was carried out overnight at 60°C. Probes were detected using a Phosphorimager plate and the probe sequences are annotated in Table S3.

RNA extraction and quantitative RT-qPCR

For *in vitro* experiments, total RNA was extracted using TRIzol (Invitrogen) followed by RNA column purification using the RNA Pure-Link Kit (Ambion). Briefly, cells were scraped from cell culture dishes and homogenized by pipetting in TRIzol solution. After phase separation with chloroform, the RNA from the aqueous phase was purified with the RNA PureLink Kit and quantified by Nanodrop spectrophotometer. cDNA was produced with the High-Capacity cDNA Reverse transcription Kit (Applied Biosystems) following manufacturer's instructions.

To analyze gene expression changes RT-qPCR was performed using 5 ng of cDNA per each real-time qPCR well. Real-time qPCRs were performed with TaqMan assays (Applied Biosystems) and TaqMan Universal PCR Master Mix in triplicates following manufacturer's instructions (Applied Biosystems 4369016). Gene expression levels were normalized using the endogenous control *PPIA* and *B2M* for each sample and differences in target gene expression were determined using SDS 2.4 or StepOne 2.2 plus software. Error bars represent standard deviation of samples performed in triplicate. The following TaqMan assays were used: EGFP (Mr04097229_mr), Tomato-BGHPA (custom made probe; F: GGGCATGGCACCAGCAGCACC, R: CCTACTTGTACAGCTCGTCCA TGCC), LGR5 (Hs00173664_m1), *ASCL2* (Hs00270888_S1), *SMOC2* (Hs0159663_m1), *MUC2* (Hs03005094_m1), *KRT20* (Hs00300643_m1), *POLR1A* (Hs00209909_m1), *POLR1B* (Hs00219263_m1), *POLR1C* (Hs01561269_g1), *RRN3* (*TIF1A*) (Hs04398176_m1), pre-5'ETS-rRNA (custom), *AscI2* (Mm01268891_g1), *Lgr5* (Mm0043889_m1), *Muc2* (Mm01276696_m1), *Smoc2* (Mm00491553_m1), and *Krt20* (Mm00508106_m1). All real-time qPCRs were normalized to *B2M* (Hs99999907_m1), *b2m* (Mm00437762_m1), *PPIA* (Hs99999904_m1), and *Ppia* (Mm02342430_g1).

Protein extraction and western blot analysis

Cells were washed twice with cold PBS and scraped with lysis buffer 1:1:1 (1 mM EDTA, 1 mM EGTA, 1% SDS) supplemented with protease and phosphatase inhibitors (Sigma Aldrich) and heated at 99°C for 10 min. Cell lysates were pipetted several times to break gDNA and later centrifuged at 13200 rpm at 4°C for 15 min. The supernatant was kept as the protein extract. Protein content was quantified with the Protein Assay (BioRad) based on the Bradford method. Equal amounts of protein per sample were separated by standard SDS-PAGE and transferred to PVDF membranes (Millipore). The membranes were incubated in TBS-T (20mM Tris, 150mMNaCl, 0.2% Tween 20) supplemented with 5% milk for 30 min at RT to block unspecific antibody binding. Primary antibodies RPA194 (*POLR1A*) (Santa Cruz, SC-48385) 1:500, *RRN3* (Sigma HPA049837) 1:500, *KRT20* (DAKO M701929-2) 1:500, *Actin* (Abcam

ab20272), 1:15000 were incubated overnight at 4°C. Secondary antibodies were diluted 1:10000 and incubated for 1 h at RT with the PVDF membranes. Membranes were washed 3 times with TBS-T 0.2% for 10 min, incubated for 5 min with SuperSignal West Pico Chemiluminescent Substrate (Thermo Scientific, 34080), and visualized using Odyssey Fc Imaging system (Li-COR).

In vitro click chemistry, in-gel fluorescence, IP

Cells were lysed with 2% SDS, extracts were quantified and diluted to 1% SDS, and 100 µg of protein was subjected to click reaction using Click-it Kit (Thermo Fisher) and IRDye 800CW Azide Infrared Dye (Li-COR). Samples were incubated in dark at room temperature for 1.5 h, and subsequently, the proteins were precipitated using standard methanol/chloroform protocol. Pellets were air-dried and re-suspended in 1% SDS. 20 µg of protein were boiled with sample buffer and loaded onto SDS-PAGE gel for further analysis of inputs or were incubated with antibody against KRT20 (Atlas antibodies, HPA024309) overnight at 4°C with shaking. The next day, protein A beads were added, and samples were incubated 1 h under same conditions. Subsequently, after extensive washes, samples were boiled with sample buffer and loaded onto SDS-PAGE gel followed by standard WB protocol. In order to detect KRT20, membranes were incubated for 1 h in dark at room temperature with 1:5000 Goat anti-Rabbit Alexa Fluor 680 (Thermo Fisher). Membranes were washed 3 times with TBS-T 0.2% for 10 min and visualized using Odyssey Fc Imaging system (Li-COR).

Analysis of protein and RNA synthesis by flow cytometry and microscopy

To measure protein synthesis *in vivo* mice were injected intraperitoneally with either 1 mg of OP-P (O-propargyl-puromycin) (Medchem Source LLP, JA-1024) or 2 mg of HPG (L Homopropargylglycine) (Click Chemistry Tools, 1067-100) per animal two hours before sacrifice. To measure RNA synthesis *in vivo* mice were injected i.p. with 4 mg EU (5-Ethynyl Uridine) (Click Chemistry Tools, 1261-100) per animal two hours before sacrifice. Subcutaneous xenografts were collected and further processed for histology or flow cytometry analysis following standard protocols. FACS Aria Fusion flow cytometer (Beckton Dickinson) was used and data were analyzed using FlowJo software. Using a Click-It kit (Thermo Fisher, C10457, C10428, C10329) OP-P, HPG or EU were conjugated to a fluorochrome in tissue sections prior to antibody staining or in FACS sorted cells which were fixed in PFA 4% for 15 min at RT before Click-It reaction. Samples were then analyzed by microscopy or flow cytometry in each case. Samples from non-injected mice were used to determine background signal. In order to measure protein or RNA synthesis *in vitro*, either OP-P (20 µM), HPG (50 µM) or EU (1 mM) was added to the medium. Cells were incubated for 2h, then trypsinized to single cell state for flow cytometry analysis, fixed, and labeled by standard Click-It reaction protocol. For microscopy analysis, cells or organoids were washed two times with PBS after the incubation period, fixed and subjected to Click-It reaction under the same conditions as stated before. When indicated, samples were stained with antibodies and further processed following a standard immunofluorescence protocol.

Xenografts disaggregation and cell isolation

Xenografts were resected and disaggregated as previously described in [Merlos-Suárez et al. \(2011\)](#) and [Cortina et al. \(2017\)](#). Human epithelial cells from disaggregated PDX were first incubated 30 min at 4°C with 1:200 CD16/CD32 (mouse, Tonbo Biosciences, 70-0161-U500) to block free antibody binding sites and with 1:200 BV421-CD31 (rat, BD Biosciences, 562939cloneMEC13.3) and 1:200 BV421-CD45RB (rat, BD Biosciences, 562849clone16A) to stain for immune and endothelial mouse cells. After this period, 1:150 EPCAM-PeCy7 (human, eBioScience 25- 9326-42) or 1:100 EPCAM-APC-Vio770 (human, Miltenyi Biotec 130-101-161) was added and incubated for 1 h at 4°C. Mouse tumor cells from AKP xenografts were stained with 1:300 EPCAM-APC-Cy7 (mouse, Biolegends, 118217 cloneG8.8). DAPI (1 µg/ml) was added to distinguish live/dead cells. The cell suspension was analyzed with a BD Fusion FACS or Aria FACS.

Generation of POLR1A and LGR5 signatures

The POLR1A and LGR5 gene signatures used for the single cell RNA-seq analysis were generated by FACS purification of high and low or negative fluorescent tumor cells from subcutaneously injected POL-iCT or LGR5-iCT knock-in PDO7. The LGR5 signature included bona fide ISC genes that were coregulated with LGR5 according to the scRNaseq data. All gene signatures used in this study are provided in [Table S5](#).

Microarrays

RNA from 2000 cells from each condition was extracted and retrotranscribed to cDNA as described in [Gonzalez-Roca et al. \(2010\)](#). The cDNA was amplified and purified using PureLink Quick PCR Purification Kit (Invitrogen). Quantification of amplified cDNA was done on a Nanodrop ND-1000 spectrophotometer (Thermo-Fisher Scientific, Waltham, MA, USA). 8 µg of the cDNA from each sample were fragmented and labeling with GeneChip Mapping 250 K Nsp assay kit (Affymetrix) following manufacturer instructions. Finally, hybridization was performed using the GeneChip Hybridization, Wash and Stain Kit (Affymetrix). Samples ready to hybridize were denatured at 99°C for 2 min prior to incubation into GeneChip Human PrimeView arrays (Affymetrix). Hybridization was performed for 16 h at 45°C / 60 rpm in GeneChip Hybridization Oven 645 (Affymetrix). Washing and Stain steps after hybridization were performed in GeneChip Fluidics Station 450 (Affymetrix), following the specific script for PrimeView arrays. Finally, arrays were scanned with GeneChip Scanner GCS3000 (Affymetrix) using default parameters, and generation of Cel files for bioinformatics analysis was done with Command Console software (Affymetrix).

Cell sorting and libraries preparation for Single-cell RNA-seq

PDO7 was infected with a CMV-CherryLuc lentiviral vector. Positively infected cells were sorted, expanded for two passages, and injected subcutaneously in a Beige nude mouse (200,000 cells in small organoid format per flank in 100 μ l BME2-HBSS). When PDX were at a mean 100 m³ volume the animal was sacrificed and xenografts were disaggregated as described before. Cherry positive alive cells from two xenograft biological replicates were sorted in single cell format in 96-well plate with Smart-seq2 lysis buffer and frozen prior to their sequencing. For PDO-p18, 2 million cells were injected subcutaneously. 100 m³ xenografts were extracted from the NSG injected animal after its sacrifice, disaggregated and stained for 1h on ice with hEpcam-APC-770 antibody (human, Milteny Biotec, 130-101-161) at 1:150 dilution after 30 min of mouse antigen blocking stain with 1:100 mCD16/CD32 (Tonbo Biosciences, 70-0161-U500), 1:100 mCD31-vio450 (BD biosciences, 562939cloneMEC13.3) and 1:100 mCD45-vio450 (BD biosciences, 562849clone16A). Epcam positive human cells from two different replica xenografts were sorted in single cell format 96MW plates with Smart-seq lysis buffer.

Full-length single-cell RNA sequencing libraries were prepared using the Smart-seq2 protocol (Picelli et al.) with minor modifications. Briefly, 96-well plates containing sorted cells in lysis buffer were reverse transcribed using SuperScript II (Invitrogen) in the presence of oligo-dT30VN, template-switching oligonucleotides and betaine. The cDNA was amplified using the KAPA HiFi Hotstart ReadyMix (Kappa Biosystems), ISPCR primer and 22 cycles of amplification. Following purification with Agencourt Ampure XP beads (Beckmann Coulter), product size distribution and quantity were assessed on a Bioanalyzer using a High Sensitivity DNA Kit (Agilent Technologies). 140 pg of the amplified cDNA were fragmented using Nextera[®] XT (Illumina) and amplified with indexed Nextera[®] PCR primers. Products were purified twice with Agencourt Ampure XP beads and quantified again using a Bioanalyzer High Sensitivity DNA Kit. Sequencing of Nextera[®] libraries from 384 cells was carried out in one lane on an Illumina HiSeq2500 v4.

QUANTIFICATION AND STATISTICAL ANALYSES

General quantifications

For ribosomal content/KRT20 ratio quantification in primary patient samples, scanned images were processed for quantification using Qupath software (<https://qupath.github.io/>). The epithelial area was selected and fragmented into 100 μ m² tiles. Mean intensity for the red and green channels was measured for each tile, and the values were represented using a scatterplot. Consecutive slides for 8 representative samples were stained for EPHB2 and 5.8S as a control. Densities of absolute-valued Log₂ ratios were used to perform statistical analysis.

To quantify the number of KRT20 and tdTomato positive cells from the KRT20 lineage tracing experiment, images were processed using Qupath as described above and the Cell detection algorithm from the same software was used. Nuclei were detected by using the DAPI channel with default nuclei parameters and tdTomato in the 568 channel. The mean intensity of KRT20 staining was measured for each tdTomato positive detected cell.

For Ki67 quantification images were processed for quantification using Qupath. In order to compare the amount of Ki67 positive cells in tumor center compared to tumor periphery, we selected 4 areas within each image: a center, and three zones representing inner (P3), outer (P2), and the outermost periphery (P1). Epithelial tumor cells were classified as positive or negative based on mean DAB nuclear intensity, and percentage of positive tumor cells within each zone was represented.

ImageJ was used for the quantification of whole slide images of tissue sections stained for KRT20 or Alcian blue. For KRT20 quantification, epithelial tumor cells were first selected as EPCAM+ and then we quantified the KRT20+ area within the epithelial compartment. Percentage of Alcian blue area represents a ratio between Alcian blue+ area and the total area of the tumor.

Quantification of the nuclear area occupied by POLR1A signal was done with ImageJ using a Macro developed by the microscopy facility at IRB.

Clonal quantification for *in vivo* lineage tracing

We tested several tamoxifen doses and assessed the % of recombination by flow cytometry in dissociated xenograft. A tamoxifen dose of 250 mg/Kg in LGR5-creERT2 PDOs, 10 mg/Kg in PORLR1A-creERT2 and 1 mg/Kg in KRT20-creERT2 triggered recombination in 1%–2% of tdTomato+ cells in the viable epithelial fraction. We corroborated this result by histology. Mice were inoculated subcutaneously with 200,000 PDO cells and treated with the indicated doses of tamoxifen when xenografts reached 50-70 mm³ (approximately 3 weeks after the inoculation). Tumors were processed for histology at indicated time points. A minimum of 4 tumor xenografts per Cre line was analyzed. Tumors were cut in half and oriented so that sections corresponded to the central area of the tumor. When all samples were collected, we performed immunohistochemical staining of 3 μ m histological sections as described above using the primary antibody against tdTomato (rabbit, Rockland, 600-401-379). Images for clone quantification were acquired using a NanoZoomer-2.0 as described above. All brightfield images were visualized with a gamma correction set at 1.8 with the NDP.view 2U123888-01 software (Hamamatsu). For clonal quantification, images were processed using ImageJ. Tomato positive objects were detected and thresholds were calculated automatically using Renyi Entropy function. The algorithm groups objects that reside in close proximity (< 13 pixels) so that they are considered as unique clones. Total and large clones number were relativized to the area (pixels) of the tumor section. To calculate number of cells, we estimated the size of single cells in histological sections and interpolated the number of cells per each clone and per section. The non-necrotic area included all tumor cells (epithelium and stroma) that were not necrotic and was obtained by manually training a machine learning tile classifier using QuPath software. This area was then divided by the total tumor area in order to calculate the non-necrotic fraction.

POLR1A expression analysis in colon samples from human cohort

GSE4407 dataset (Sanz-Pamplona et al., 2014) was downloaded from the NCBI GEO repository. These data include gene expression and clinical information from 50 healthy human colon mucosa along with 98 tumor CRC stage II samples and their paired adjacent morphologically normal mucosa. Raw cel files were normalized using the same procedure described below (see section Microarray analyses). Technical information concerning samples processing and hybridization was retrieved from the original CEL files: date of scanning were collected in order to define scan batches in each dataset separately; technical metrics described by Eklund AC and Szallasi Z in Eklund and Szallasi (2008) were computed and recorded as additional features for each sample. Expression data were corrected by metrics PM.IQR, RMA.IQR and RNA.DEG (Eklund and Szallasi, 2008) and by scanning day. For doing so, a linear model was fitted separately for each probeset that included these metrics as the only explanatory variables, and the coefficients of such models were used to correct the expression values a-priori. Next, the same procedure was carried out for correcting by technical effects captured by scanning date. Finally, expression intensities were summarized at the gene level (entrez) by the first principal component of the probesets mapping to the same gene. This component was centered and scaled to the weighted mean of the probesets' means and standard deviations, where the contributions to this first component were used as weights. The sign of this score was then corrected so that it was congruent to the sign of the probeset contributing the most to the first component. Association between POLR1A expression and sample type was evaluated using a linear model (Wald test). The threshold for statistical significance was set at 5%. All analyses were carried out using R and Bioconductor (Gentleman et al., 2004).

Microarray analyses

Samples were hybridized in PrimeView Human Gene Expression Array and processed with packages affy (Gautier et al., 2004) and affyPLM (Bolstad et al., 2005) from R and Bioconductor (Gentleman et al., 2004). Raw cel files were normalized using RMA background correction and summarization (Irizarry et al., 2003). Probeset annotation was performed using the information available on the Affymetrix – ThermoFisher web page (<https://www.thermoFisher.com/us/en/home/life-science/microarray-analysis/affymetrix.htm>). Accessed on 29/10/2019). Standard quality controls were performed in order to identify abnormal samples regarding: a) spatial artifacts in the hybridization process (scan images and pseudo-images from probe level models); b) intensity dependences of differences between chips (MvA plots); c) RNA quality (RNA digest plot); d) global intensity levels (boxplot of perfect match log-intensity distributions before and after normalization and RLE plots); e) anomalous intensity profile compared to the rest of the samples (NUSE plots, Principal Component Analyses); f) impact of quality metrics (Eklund and Szallasi, 2008) on expression measures. Samples from batch "cm.1509" in the tumor dataset (refers to the Ephb2 populations, Figure 1) were a priori corrected gene-wise by RMA.IQR metric (Eklund and Szallasi, 2008) using a linear model with no more covariates included in it. No samples were excluded from the study due to quality issues. Differential expression analysis was performed using a linear model with empirical shrinkage (Smyth, 2004) as implemented in the limma R package (Ritchie et al., 2015). Comparisons were controlled for biological replicate by including the sample's donors in the model as covariates. In the tumor dataset (refers to the Ephb2 populations, Figure 1), the models additionally included the tissue as covariate (Normal/Tumor) as well as the interaction between tissue and Ephb2 status. Benjamini and Hochberg False Discovery Rate (FDR) (Smyth, 2004) was used for multiple comparisons correction. Pathway enrichment analyses were performed using a modification of ROAST (Wu et al., 2010), a rotation-based approach implemented in the R package limma (Ritchie et al., 2015) that is specially suitable for small size experiments. Such modifications were implemented to accommodate the re-standardized maxmean statistic proposed in the ROAST algorithm, in order to enable it for competitive testing (Goeman and Bühlmann, 2007). For visualization purposes, we represented these results using the Enrichment Score graphic from the Gene Set Enrichment Analysis (GSEA) algorithm (Subramanian et al., 2005). Genesets derived from the KEGG pathway database (Kanehisa and Goto, 2000) and the Gene Ontology (GO) (Ashburner et al., 2000) as collected in the R package org.Hs.eg.db were used for these analyses, as well as the Broad Hallmark gene set collection from the MsigDB (Liberzon et al., 2015).

RNA-Seq data

Reads were aligned to the primary assembly of the mm10 Ensembl genome (GRCm38) using STAR (version 2.7.0a, default parameters) (Dobin et al., 2013). Quantification of count per genomic feature was performed using the R package Rsubread (Liao et al., 2013) (function featureCounts, default parameters). GO (Ashburner et al., 2000) terms were retrieved from R package org.Mm.eg.db, while Broad Hallmark sets were translated to mouse homologous genes using the R package biomaRt (Durinck et al., 2009). Expression counts were rlog-transformed (Love et al., 2014) and summarized at the gene set levels as follows: rlog-values were centered and scaled gene-wise to produce z-scores, which were then averaged across all genes included in a given gene set; the resulting score were in turn centered and scaled across samples that were included in the dataset. Expression data at the gene set level were graphically represented in a heatmap using a blue to red color gradation, where red indicated the highest expression and white corresponded to the lowest expression values. For clarity, the most extreme values were truncated to -1.5 and 1.5 .

Single-cell RNA-seq data analysis

Sequencing was carried out as paired-end (PE75) reads with library indexes corresponding to cell barcodes. After sequencing, libraries were inspected with the FastQC suite to assess the quality of the reads. Reads were then demultiplexed according to the cell barcodes and mapped on the human reference genome (Gencode release 27, assembly GRCh38 p10) with the RNA pipeline of the GEMTools (Marco-Sola et al., 2012) 1.7.0 suite using default parameters (6% of mismatches, minimum of 80% matched bases, and minimum quality threshold of > 26).

For both PDO7 and PDO-p18, cells with < 65% of mapped reads or < 100,000 of total mapped reads were discarded. Cells with > 100 genes and < 25% of mitochondrial gene counts were included in downstream analyses, resulting in read count matrices containing 511 (PDO7) and 388 (PDO18) single cells. Genes that were expressed in fewer than five cells were removed. Filtering, normalization, selection of highly variable genes (HVG) and clustering of cells were performed according to the Seurat (Satija et al., 2015) package (version 2.3.4). Selection of HVG was based on the evaluation of the relationship between gene dispersion ($y.cutoff = 0.5$) and the log mean expression ($x.high.cutoff = 3$), while the total number was limited to the mean of genes per cell. Projections of HVG onto a reduced dimensional space was used for the graph-based clustering to group cells into subpopulations. At this step, the dimension of the subspace was set to the number of significant principal components (PC); based on the distribution of the PC standard deviations. The number of clusters was aligned to the expected biological variability and cluster identities were assigned using previously described gene markers and transcriptional signatures derived from bulk RNA sequencing of the principal cell populations. T-SNE was used to visualize the clustering distribution of cells. Trajectory analysis and pseudo-ordering of cells were performed with the Monocle (Qiu et al., 2017) package (version 2.8.0) using the previously identified HVG. Cell clustering and pseudo-time were consistent between and within samples.

Single-cell RNA-Seq data – enrichment analysis

LGR5/POL1 gene expression signatures were retrieved from the scRNA-Seq differential expression analyses using different thresholds for fold-change and statistical significance. These signatures were evaluated for pathway enrichment using a hypergeometric test for their intersection with gene sets in the GO (Ashburner et al., 2000) and Hallmarks (Liberzon et al., 2015) collections.

Statistical analyses

To test statistical significance between samples from two different groups two-tailed Student's t tests were used. When comparing samples from the same animal paired t tests were applied. When comparing different groups within different variables, multiple comparison two-way ANOVA Tukey's tests were used. For Figures 1G and 4K and 4M a mixed effects linear model was fitted with technical replicates taken as random effects and PDOs as fixed effects. The "lmer" function from the lme4 (Bates et al., 2014) R package was used for fitting the model. Coefficients and p values for the comparisons of interest were computed through the "glht" function from the multcomp (Hothorn et al., 2008) R package using the "Westfall" multiplicity adjustment method. Confidence intervals for the coefficients were calculated with the "confint" function. Plots were generated using R programming language (Bunn and Korpela, 2014). Data from 5.8S and KRT20 staining of FFPE primary CRCs (Figure 3J and S3D) were represented in a smoothed scatterplot using the R function *smoothScatter* (Bunn and Korpela, 2014), where color intensity corresponded to the density of data points through a 2-dimension kernel estimate. Joint distribution of KRT20 and 5.8S values were tested against a proper set of negative control samples stained with 5.8S and EPHB2 (data not shown). Log₂-ratios of the corresponding marker against 5.8S values were computed for each stain data point. Each sample was then summarized by the median of the absolute value of these log₂-ratios. Distributions of these values for KRT20 and EPHB2 samples were then compared using a Komolgorov-Smirnov test. For Kaplan-Meier curves, Gehan-Breslow-Wilcoxon test was applied. In growth kinetics experiments statistical significance was obtained by comparing the relative tumor volume of the last measure from control subjects with the corresponding measure of treated animals in a two-tailed Student's t test. All group data are represented by the mean and errors bars are the standard error of the mean (s.e.m) and statistical tests and plots were generated with GraphPad Prism unless indicated.

Sample sizing and collection

All samples and animals were assigned randomly to experimental conditions, as well as sample collection. Automated quantifications and blind data analysis were done whenever possible. A minimum of three representative images were quantified in each experiment and each condition.